

The origin and evolution of r- and s-process elements in the Milky Way stellar disk^{★,★★}

Chiara Battistini^{1,2} and Thomas Bensby¹

¹ Lund Observatory, Department of Astronomy and Theoretical Physics, Box 43, SE-221 00, Lund, Sweden

² current address: Zentrum für Astronomie der Universität Heidelberg, Landessternwarte, Königstuhl 12, 69117 Heidelberg, Germany
e-mail: cbattistini@lsw.uni-heidelberg.de

Received 16 September 2015 / Accepted 2 November 2015

ABSTRACT

Context. Elements heavier than iron are produced through neutron-capture processes in the different phases of stellar evolution. Asymptotic giant branch (AGB) stars are believed to be mainly responsible for elements that form through the *slow* neutron-capture process, while the elements created in the *rapid* neutron-capture process have less understood production sites. Knowledge of abundance ratios as functions of metallicity can lead to insights on the origin and evolution of our Galaxy and its stellar populations.

Aims. We aim to trace the chemical evolution of the neutron-capture elements Sr, Zr, La, Ce, Nd, Sm, and Eu in the Milky Way stellar disk. This will allow us to constrain the formation sites of these elements as well as to probe the evolution of the Galactic thin and thick disks.

Methods. Using spectra of high resolution ($42\,000 \leq R \leq 65\,000$) and high signal-to-noise ($S/N \geq 200$) obtained with the MIKE and FEROS spectrographs, we determine Sr, Zr, La, Ce, Nd, Sm, and Eu abundances for a sample of 593 F and G dwarf stars in the Solar neighbourhood. The abundance analysis is based on spectral synthesis using one-dimensional, plane-parallel, local thermodynamic equilibrium (LTE) model stellar atmospheres calculated with the MARCS 2012 code.

Results. We present abundance results for Sr (156 stars), Zr (311 stars), La (242 stars), Ce (365 stars), Nd (395 stars), Sm (280 stars) and Eu (378 stars). We find that Nd, Sm, and Eu show trends similar to what is observed for the α -elements in the $[X/Fe]$ - $[Fe/H]$ abundance plane. For $[Sr/Fe]$ and $[Zr/Fe]$ we find decreasing abundance ratios for increasing metallicity, reaching sub-solar values at super-solar metallicities. $[La/Fe]$ and $[Ce/Fe]$ do not show any clear trend with metallicity, being close to solar values at all $[Fe/H]$. The trends of abundance ratios $[X/Fe]$ as a function of stellar ages present different slopes before and after 8 Gyr.

Conclusions. The rapid neutron-capture process is active early in the Galaxy, mainly in type II supernovae from stars in the mass range $8-10 M_{\odot}$. Europium is almost completely produced by r-process but Nd and Sm show similar trends to Eu even if their s-process component is higher. Strontium and Zr are thought to be mainly produced by s-process, but show significant enrichment at low metallicity that requires extra r-process production, that probably is different from the classical r-process. Finally, La and Ce are mainly produced via s-process from AGB stars in mass range $2-4 M_{\odot}$, which can be seen by the decrease in $[La/Eu]$ and $[Ce/Eu]$ at $[Fe/H] \approx -0.5$. The trend of $[X/Fe]$ with age could be explained by considering that the decrease in $[X/Fe]$ for the thick disk stars can be due to the decrease of type II supernovae with time meaning a reduced enrichment of r-process elements in the interstellar medium. In the thin disk the trends are flatter that probably is due to that the main production from s-process is balanced by Fe production from type Ia supernovae.

Key words. Stars: abundances – Stars: solar-type – Galaxy: disk – Galaxy: evolution – Galaxy: solar neighborhood

1. Introduction

Elements with atomic numbers up to iron can be synthesised via nuclear fusion in the interiors of stars. Heavier elements are formed by the addition of neutrons in the stellar interiors, and are called neutron-capture elements. There are two main ways to add neutrons, through *slow* neutron-capture (s-process), or through *rapid* neutron-capture (r-process), depending on if the neutron-capture is slow or rapid compared to the timescale for β^- decay (Burbidge et al. 1957). The s-process requires a low neutron flux

and the creation of the new elements moves along the valley of β stability. In the case of the r-process, the neutron flux is intense, permitting the creation of elements outside the valley of stability.

An important step in the study of neutron-capture elements was the discovery that metal-poor stars show high relative abundances of certain neutron-capture elements compared to Fe, meaning that the r- and s-processes were already active at early times (e.g. Frebel & Norris 2013). In particular for the r-process, this was by the significant number of stars with high levels of the r-process element Eu at very low metallicities (e.g. the neutron-capture review by Sneden et al. (2008)). However, the production sites for r-process elements are poorly understood and currently there are at least three possible scenarios. First, the classic scenario for r-process production is neutrino-induced winds from type II supernovae (SN II) (Woosley et al. 1994). Extremely energetic neutrinos are produced during the collapse of the SN II and they are potentially able to interact with the dense material

* This paper includes data gathered with the 6.5 meter Magellan Telescopes at the Las Campanas Observatory, Chile and the ESO 1.5-m, 2.2-m, and 3.6-m telescopes on La Silla, Chile (ESO Proposal ID 65.L-0019, 67.B-0108, 76.B-0416, 82.B-0610); and data from UVES Paranal Observatory Project (ESO DDT Program ID 266.D-5655).

** Tables 3 and 4 are only available at the CDS via anonymous ftp to cdsarc.u-strasbg.fr (130.79.128.5) or via <http://cdsarc.u-strasbg.fr/viz-bin/qcat?J/A+A/XXX/XXX>

that is falling onto the core of the star. This interaction can heat the material giving to it the additional energy necessary to recreate the energy output observed of $\approx 10^{51}$ ergs. Another scenario is the merging of neutron stars (Freiburghaus et al. 1999), or the merging of a neutron star with a black hole (Surman et al. 2008). Rosswog et al. (2014) shows that that dynamic ejecta from this merging produce r-process elements with $A > 130$ with a pattern independent from the kind of merging, while neutrino-driven winds are responsible for nucleosynthesis of elements from $A = 50$ to $A = 130$ but in this case the exact output depends on the merging parameters. Lastly, polar jets from SN II with the use of a pure magnetohydrodynamic explosion seems to lead to the right conditions to have r-process nucleosynthesis (Nishimura et al. 2006). Unfortunately there are still theoretical problems in the modelling of SN II explosions with neutrino wind that prevent a definitive confirmation of the latter production site. In addition to this, theoretical predictions for r-process production have not been entirely successful in synthesising the observed total abundance distribution of r-process nuclei (Cescutti et al. 2006).

The production of s-process elements, on the other hand, can occur both in massive stars, in the He-burning core, and in the convective C-burning shell (Pignatari et al. 2010), as well as in asymptotic giant branch (AGB) of lower mass stars at solar and lower metallicities (Bisterzo et al. 2011). Considering that the s-process is responsible for the production of approximately half of the nuclides from Fe to Bi, in particular feeding the groups Sr-Y-Zr, Ba-La-Ce-Pr-Nd, and Pb, understanding how and where the s-process elements are produced is very important. However, our understanding is poor, especially in respect to the where, when, and how much of these elements is produced. Abundance surveys of metal-poor dwarf stars in the halo revealed the presence of very old stars that are extremely rich in s-process elements (Snedden et al. 2008). These high abundances are difficult to explain with stellar evolution and nucleosynthesis theories because dwarf stars on the main-sequence cannot produce these elements. However, if a dwarf star experienced accretion from a more massive giant companion the peculiar atmospheric abundance of the dwarf star can be explained. In fact, if the giant companion already experienced dredge-up, bringing s-process elements produced during its AGB phase to the surface, these elements can be transferred onto the dwarf companion (Aoki et al. 2001).

Most neutron-capture elements can be produced by both s- and r-processes, and it is not always easy to constrain which of the processes that are involved in the creation path(s) of each element. An important work on the production rates for neutron-capture elements was the one from Arlandini et al. (1999). They claim that the s-process production is responsible for 85 % of Sr abundance, 83 % of Zr, 62 % of La, 77 % of Ce, 30 % of Sm, and only 7 % of Eu. Thanks to its very limited s-process component, Eu is considered a “pure” r-process element and is well suited for determining the corresponding r-process contribution for other elements (Winckler et al. 2006). For Nd, the production is equally divided between the s- and r-processes (56 % produced by s-process). Since Arlandini et al. (1999) several works have derived new production rates and yields for the neutron-capture elements, including better cross-section measurements for the reactions and evolutionary model for stars of different metallicities and masses. However, large uncertainties are still present in the s- and r-process calculations (Karakas 2014). At the same time, observations usually show spread in abundances at a given metallicity and this can be due to the dependence of neutron-capture process on metallicity (Travaglio et al. 2004).

Table 1: Analysed elements and spectral lines.[†]

Element	λ [Å]	EP [eV]	Isotopic ratio	Reference
Sr I	4607	0.00	⁸⁴ Sr 0.56 %	Bautista et al. (2002)
			⁸⁶ Sr 9.86 %	
			⁸⁷ Sr 7.00 %	
			⁸⁸ Sr 82.58 %	
Zr II	4208	0.71	⁹⁰ Zr 51.45 %	Ljung et al. (2006)
Zr I	4687	0.73	⁹¹ Zr 11.22 %	
Zr I	4739	0.65	⁹² Zr 17.15 %	
Zr II	5112	1.66	⁹⁴ Zr 17.38 % ⁹⁶ Zr 2.38%	
La II	4662	0.00	¹³⁸ La 0.09 %	Ivans et al. (2006)
La II	4748	0.93	¹³⁹ La 99.91 %	
La II	5122	0.32		
La II	6390	0.32		
Ce II	4523	0.68	¹³⁶ Ce 0.19 %	Lawler et al. (2009)
Ce II	4572	0.68	¹³⁸ Ce 0.25 %	
Ce II	4628	0.52	¹⁴⁰ Ce 88.45 %	
Ce II	5187	1.21	¹⁴² Ce 11.11 %	
Nd II	4177	0.06	¹⁴² Nd 27.20 %	Roederer et al. (2008)
Nd II	4358	0.32	¹⁴³ Nd 12.20 %	
Nd II	4446	0.20	¹⁴⁴ Nd 23.8 %	
Nd II	5130	1.30	¹⁴⁵ Nd 8.30 %	
Nd II	5319	0.55	¹⁴⁶ Nd 17.20 %	
			¹⁴⁸ Nd 5.70 % ¹⁵⁰ Nd 5.60 %	
Sm II	4467	0.66	¹⁴⁴ Sm 3.07 %	Lawler et al. (2006) Roederer et al. (2008)
Sm II	4523	0.43	¹⁴⁷ Sm 14.99 %	
Sm II	4577	0.25	¹⁴⁸ Sm 11.24 %	
Sm II	4669	0.28	¹⁴⁹ Sm 13.82 %	
			¹⁵⁰ Sm 7.38 %	
			¹⁵² Sm 26.75 % ¹⁵⁴ Sm 22.75 %	
Eu II	4129	0.00	¹⁵¹ Eu 47.80 % ¹⁵³ Eu 52.20%	Lawler et al. (2001)

Notes. ([†]) Column 1 shows the name of the element and the ionisation stage. The wavelength and the energy potential for the different lines are listed in columns 2 and 3, respectively. Column 4 shows the isotopic ratio while column 5 give the references for the different elements.

The relative contribution from each of the processes to the abundance of an element and to the various abundance ratios change during the evolution of the Galaxy. This means that a complete overview of the stellar populations at different metallicities is needed for a better understanding of the evolution of these elements. Considering the possible production sites listed above, and that the first low-mass stars in the Universe reached their AGB phase about 500 millions of years after the Big Bang (see for example Snedden et al. 2008), the s-process enrichment occurs with some delay with respect to SNII, that start to explode after few millions years after the onset of star formation. The study of this delay and how the different elemental abundances relate to each other at different metallicities can help us to understand the evolution of the Galactic disk. For this purpose, dwarf stars are very suitable because they have very long lifetimes, comparable to the age of the Universe (Sackmann et al. 1993) and their surface abundance can be considered to be representative of the chemical composition of the gas cloud they were born from (Lambert 1989; Freeman & Bland-Hawthorn 2002). This means that the information that can be derived from these

types of stars are directly related to the enrichment processes happened in the previous stellar generations, all the way back to the first billion years of the Milky Way history.

In this paper we derive abundances of some neutron-capture elements (Sr, Zr, La, Ce, Nd, Sm, and Eu) in the Solar neighbourhood and in addition to this, in our investigation, we made use of the abundances of Ba derived by [Bensby et al. \(2014\)](#). Even if the method used is not the same (for Ba was used equivalent width measurements), one of the scope of this paper is to analyse elements that were not studied in [Bensby et al. \(2014\)](#).

The paper is organised as follow: In Sect. 2 the stellar sample and the abundance analysis are described. Section 3 give the abundance results for Sr, Zr, La, Ce, Nd, Sm, and Eu. Section 4 discusses possible origins of these neutron-capture elements and their evolution in the Milky Way. Finally, Sect. 6 summarises our findings.

2. Abundance analysis

2.1. Stellar sample and stellar parameters

The stars in this study are a subset of the 714 F and G dwarf star sample of [Bensby et al. \(2014\)](#), namely those 593 stars observed with the FEROS and MIKE high-resolution spectrographs that have complete wavelength coverage from about 3500 to above 9000 Å. This is important as many of the spectral lines that we utilise are located in the blue spectral region. The spectra have spectral resolutions between $R = 48\,000$ to $65\,000$ and the signal-to-noise ratios are generally greater than $S/N > 200$. Further details are given in [Bensby et al. \(2014\)](#).

Stellar parameters, ages, and elemental abundances for O, Na, Mg, Al, Si, Ca, Ti, Cr, Fe, Ni, Zn, Y, and Ba were determined for all 714 stars in [Bensby et al. \(2014\)](#) where the reader is directed for full details. Briefly, the determination of stellar parameters was performed by requiring excitation balance of abundances from Fe I lines for the effective temperature (T_{eff}), ionisation balance between Fe I and Fe II lines for surface gravity ($\log g$), and that abundances from Fe I lines are independent of reduced line strength to get microturbulence parameter (ξ_t). Stellar ages were determined using a grid of α -enhanced Yonsei-Yale isochrones by [Demarque et al. \(2004\)](#) using probability distribution functions as explained in [Bensby et al. \(2014\)](#). In short, the age probability distribution of each star is constructed considering the errors in effective temperature, surface gravity and metallicity of that specific star, that permit to derive a most likely age for the stars (and these ages are the ones used in the paper) together with a lower and higher estimation (used to calculate the errors on the ages). In addition, Sc, V, Mn, and Co abundances were determined in [Battistini & Bensby \(2015\)](#) for part of the sample.

2.2. Spectral line synthesis

The spectral lines from the heavy neutron-capture elements are usually located in the blue regions of the visible spectrum. The blue region is very crowded with spectral lines, and especially so for metal-rich disk stars, meaning that blends from other species are frequent. The crowdedness of the blue spectral regions also make the placement of the continuum difficult. In addition, heavy elements usually consist of several isotopes and their spectral lines can be affected by hyperfine splitting. Therefore, to determine abundances from these lines one has to use spectral line synthesis in order to accurately account for wave-

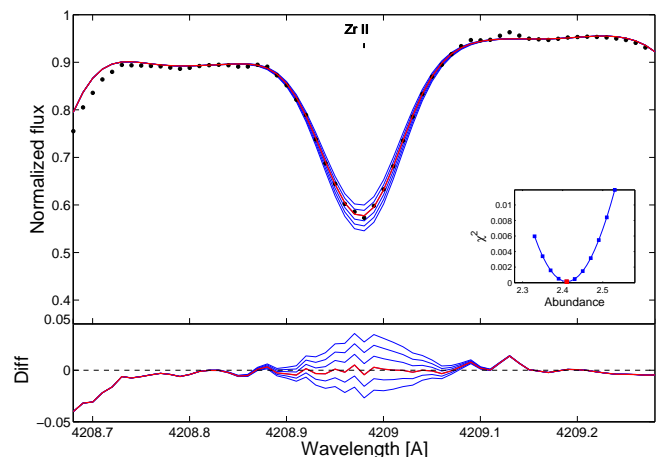


Fig. 1: Synthesis of the Zr II line at 4208 Å in the solar spectrum (in this case Vesta, observed with the MIKE spectrograph in January 2006). The upper panel shows synthetic spectra with different Zr abundances in steps of 0.04 dex (blue lines). The difference between the observed spectrum and the synthetic spectra is plotted in the lower panel with the best abundance spectrum plotted as a red line in both the upper and lower panel. The inset shows the χ^2 fit to determine the best abundance value expressed as $\log \epsilon(\text{Zr})$ (shown as a red dot).

length shifts of the different isotopes, hyperfine components, and other blending features.

Table 1 lists the spectral lines that we use in this study. It shows the analysed lines with the isotopic ratios of the elements, ionisation stages, wavelengths, and excitation potential together with reference work where these details were gathered. For Sm and Nd, that suffer in large part by isotopic shifts and also hfs, we use data from [Roederer et al. \(2008\)](#), for La we used hfs only components from [Ivans et al. \(2006\)](#) since La has only one naturally-occurring isotope, and for Eu we used shifts correction for isotopic and hfs substructures from [Lawler et al. \(2001\)](#). However, some of the lines of the elements affected by hfs are anyway treated as single lines because the wavelength splitting is small enough to be ignored. In our linelists the lines treated as single lines are La II at 4748 Å, Nd II at 5130 Å and at 5319 Å, and Sm II at 4523 Å, 4577 Å, and 4669 Å. All lines from Sr II, Zr II and Ce II lines are treated as single lines since there is no information in literature on their hyperfine structure and isotopic shifts or because they do not suffer of these problems. Atomic data for blending lines and other nearby lines were taken from the compilation available in the Vienna Atomic Line Database (VALD, [Piskunov et al. 1995](#); [Ryabchikova et al. 1997](#); [Kupka et al. 1999, 2000](#)). The complete linelists with hyperfine components can be found in Appendix A.

2.3. Abundance determination

The methodology for abundance determination is the same as in [Battistini & Bensby \(2015\)](#) where we analysed Sc, V, Mn, and Co for the same sample of stars. It is based on comparisons between observed spectra and synthetic spectra to find the best fitting abundance. The synthetic spectra were calculated with the MARCS2012 code ([Gustafsson et al. 2008](#)), under the assumption of local thermodynamic equilibrium (LTE), and one-dimensional plane-parallel model atmospheres.

Table 2: Elemental abundances for individual lines in the solar spectrum.[†]

Line	FEROS $R = 48\,000$	MIKE 1 $R = 65\,000$	MIKE 2 $R = 65\,000$	MIKE 3 $R = 65\,000$	MIKE 4 $R = 42\,000$	<MIKE>	σ <MIKE>	Solar abundance from Asplund et al. (2009)
Sr 4607	2.92	2.76	2.62	2.78	2.61	2.69	0.09	2.87 ± 0.07
Zr 4208	2.39	2.42	2.44	2.42	2.35	2.44	0.06	2.58 ± 0.04
Zr 4687	2.43	2.55	2.48	2.52	2.43	2.50	0.05	
Zr 4739	2.39	2.57	2.47	2.57	2.46	2.52	0.06	
Zr 5112	2.57	2.54	2.48	2.51	2.45	2.50	0.04	
La 4662	1.31	1.21	1.29	1.36	1.38	1.31	0.08	1.10 ± 0.04
La 4748	1.22	1.28	1.38	1.22	1.19	1.27	0.08	
La 5122	1.10	1.11	1.18	1.14	1.21	1.16	0.05	
La 6390	1.10	1.23	1.23	1.12	1.15	1.18	0.06	
Ce 4523	1.55	1.65	1.70	1.70	1.62	1.67	0.07	1.58 ± 0.04
Ce 4572	1.72	1.70	1.68	1.80	1.65	1.71	0.07	
Ce 4628	1.70	1.66	1.72	1.72	1.60	1.68	0.06	
Ce 5187	1.48	1.45	1.45	1.36	1.38	1.41	0.05	
Nd 4177	1.33	1.45	1.49	1.45	1.41	1.45	0.03	1.42 ± 0.04
Nd 4358	1.62	1.76	1.64	1.66	1.62	1.67	0.06	
Nd 4446	1.30	1.38	1.43	1.38	1.36	1.39	0.03	
Nd 5130	1.44	1.61	1.61	1.57	1.49	1.57	0.06	
Nd 5319	1.28	1.25	1.25	1.31	1.33	1.29	0.04	
Sm 4467	0.83	0.85	0.93	0.92	0.84	0.89	0.05	0.96 ± 0.04
Sm 4523	0.84	0.93	1.00	1.00	0.99	0.98	0.04	
Sm 4577	0.91	1.04	1.00	0.93	0.95	0.98	0.05	
Sm 4669	1.25	1.25	1.22	1.33	1.40	1.30	0.08	
Eu 4129	0.34	0.34	0.48	0.41	0.33	0.39	0.07	0.52 ± 0.04

Notes. ^(†) Columns 2-6 list the single abundances for the different instruments and resolutions. Columns 7 and 8 show the median abundance values for MIKE spectra for the different observation runs and the one σ dispersion, respectively. The mean abundances are used as solar abundance for MIKE spectra observed in the run with $R = 55\,000$ (see Table 1 in [Bensby et al. 2014](#)) since no solar spectra is available in this setting. In col. 9 are listed the solar abundances values from [Asplund et al. \(2009\)](#).

Table 3: Abundance from single lines.[†]

HIP	$\epsilon(\text{Sr})$		$\epsilon(\text{Zr})$				$\epsilon(\text{La})$				$\epsilon(\text{Ce})$				$\epsilon(\text{Nd})$					$\epsilon(\text{Sm})$				$\epsilon(\text{Eu})$
	4607	4208	4687	4739	5112	4662	4748	5122	6390	4523	4572	4628	5187	4177	4358	4446	5130	5319	4467	4523	4577	4669	4129	
80	2.06	1.95	–	–	1.97	–	–	–	–	–	1.00	0.96	–	–	–	–	1.05	0.80	0.53	–	–	–	–	0.12
305	–	2.51	–	–	–	1.51	–	–	–	1.75	1.95	–	1.65	–	1.72	–	–	1.38	–	–	–	–	–	0.52
407	–	2.56	2.75	–	–	–	1.32	–	1.26	1.71	–	1.78	1.63	–	1.71	–	1.68	1.35	–	1.07	–	–	–	0.47
⋮	⋮	⋮	⋮	⋮	⋮	⋮	⋮	⋮	⋮	⋮	⋮	⋮	⋮	⋮	⋮	⋮	⋮	⋮	⋮	⋮	⋮	⋮	⋮	⋮

Notes. ^(†) Abundances from the single line analyzed in this work. The table is only available in electronic form at the CDS.

Table 4: Stellar parameters and abundance results for the entire sample.[†]

HIP	T_{eff}	$\log g$	[Fe/H]	ξ_t	[Sr/H]	[Zr/H]	[La/H]	[Ce/H]	[Nd/H]	[Sm/H]	[Eu/H]
80	5856	4.1	-0.59	1.12	-0.72	-0.53	–	-0.73	-0.52	-0.39	-0.29
⋮	⋮	⋮	⋮	⋮	⋮	⋮	⋮	⋮	⋮	⋮	⋮

Notes. ^(†) The table is only available in electronic form at the CDS

The synthetic spectra were created using SME (Spectroscopy Made Easy, [Valenti & Piskunov \(1996\)](#); [Valenti & Fischer \(2005\)](#)) with stellar parameters from [Bensby et al. \(2014\)](#) as input. The abundance analysis is done through a minimisation routine of an un-normalised χ^2 function based on the difference between the observed and the synthetic spectra. An example of

the comparison between observed and synthetic spectra can be seen in Fig. 1 for the Zr II at 4208 Å in one of the available solar spectra. In Table 2 the abundances from individual lines are listed for the different solar spectra that we analysed. The fewer abundances usually available for La are due to the fact that the

lines are generally weak so more similar to the spectral noise, while for Sr the line is in most cases not well synthesized.

The analysis was done strictly differentially with respect to the Sun. The solar spectra for each observation run is listed in Table 1 in [Bensby et al. \(2014\)](#) and were used to determine abundances for the different lines using the same methodology as for stars in the sample. [Bedell et al. \(2014\)](#) noted that the derived abundances from different solar spectra observed with different instruments can differ by up to 0.04 dex. Hence, we decided to normalise the abundances on a line-by-line basis, using the correspondent solar spectrum from the different runs, when available. For the observation runs that do not have a solar observation an average abundance based on abundances from all solar spectra was used. Table 2 gives the abundances we derived for individual lines in the different solar spectra and Figs. B.1–B.5 in Appendix B show all line fits in one of the solar spectra, and an example is shown in Fig. 1.

A difficulty in the analysis for these elements is that most of the lines are weak, meaning that even if the signal-to-noise of the spectrum is high, in some cases the noise is comparable to the strength of the lines (this is visible in . In the solar spectrum these lines show equivalent widths ranging from few mÅ (Ce at 5187 Å, 4 mÅ, and La at 4748 Å, 5.3 mÅ) to several tens of mÅ (Eu at 4129 Å, 35.6 mÅ, Sr at 4607 Å, 44.4 mÅ, and Zr at 4208 Å, 78 mÅ). So, at the end of the fitting procedure of the each spectral line a visual inspection was performed to evaluate if the value for the best abundance from each line actually accurately reproduced the shape of the observed line. On a total of 597 stars from the FEROS and MIKE spectra, we have Sr abundances for 156 stars, Zr for 311 stars, La for 242 stars, Ce for 365 stars, Nd for 395 stars, Sm for 280 stars, and Eu for 378 stars. All abundances from individual lines are given in Table 3, while the solar-normalized averaged values are given in Table 4. When results from more than two lines are available, we use median value because it is less affected by outliers.

2.4. Systematic and random error estimation

Performing a differential analysis relative to the Sun means that systematic errors arising from uncertainties in atomic data and the analysis methods largely cancel out. To further check for systematic uncertainties we search the literature for other studies that have analysed the same stars to investigate possible offset in stellar parameters and derived abundances. Table 5 lists the differences in stellar parameters and abundances for the stars in common with [Reddy et al. \(2003, 2006\)](#), [Mashonkina et al. \(2004\)](#), [Mashonkina et al. \(2007\)](#) and [Mishenina et al. \(2013\)](#). Among the different works, we share the highest number of stars with neutron-capture abundances determination with [Reddy et al. \(2006\)](#) while for the other works, like [Reddy et al. \(2003\)](#) and [Mishenina et al. \(2013\)](#), we only have one or two stars in common, giving no real information on possible offsets. Only the comparison with [Reddy et al. \(2006\)](#) contains enough stars (more than ten) to show that in this case there is good agreement.

The estimation of the random errors for our abundances was done by deriving how much the errors in the stellar parameters would affect the final abundances. We follow the same procedure as in [Battistini & Bensby \(2015\)](#), selecting a random subsample of stars probing different part of the stellar parameters space and calculating the new abundances when the the random errors from [Bensby et al. \(2014\)](#) are applied to each star. First we calculate the difference between the abundances without and

with the errors on stellar parameters applied, then all the differences for each element are used to calculate the final square mean error. We consider an error on the abundance determination of 0.05 dex for wrong continuum placement and from not perfectly fitted lines. The list of the abundance errors together with the mean standard random errors on stellar parameters are listed in Table 6.

As it is visible in Table 6, the error on Eu is the smallest between the elements we analysed and is comparable with the errors on [Fe/H]. On average, our errors for the elements are around 0.1 dex but for Sr is higher, precisely of 0.15 dex, probably due to the fact that Sr presents high spread (as it will be explained in Sect. 3).

3. Results

3.1. General abundance trends

In this section we present the abundance results for the neutron-capture elements that we have analysed and Fig. 2 shows the [X/Fe] versus [Fe/H] abundance trends.

3.1.1. Strontium

Strontium in Fig. 2a shows increasing [Sr/Fe] abundance ratios with decreasing metallicity: [Sr/Fe] ≈ -0.2 for solar metallicity stars that reaches [Sr/Fe] ≈ 0 at [Fe/H] ≈ -1 . There are a few stars that show high [Sr/Fe] ratios, which could be due to the fact that only one Sr line was used. A similar spread is found in giant stars from [Borris et al. \(2000\)](#) and dwarf stars from [Mashonkina & Gehren \(2001\)](#), [Reddy et al. \(2003\)](#) and [Brewer & Carney \(2006\)](#) (even though they derived abundances from Sr II lines) for stars in a metallicity range similar to ours ($-2.0 \lesssim [\text{Fe}/\text{H}] \lesssim 0.2$), where the trend is on average solar. [Sr/Fe] for very metal-poor stars ($[\text{Fe}/\text{H}] < -2.5$), as for giants in [Borris et al. \(2000\)](#) and [Andrievsky et al. \(2011\)](#), presents a down-turn. We notice that [Andrievsky et al. \(2011\)](#) used NLTE values for Sr but the same trend is still present even when compared to the LTE case. In addition to literature results, more recently [Ishigaki et al. \(2013\)](#) observed stars in thick disk and halo and found solar [Sr/Fe] ratios for $[\text{Fe}/\text{H}] \lesssim -1$. In addition to literature results, more recently [Ishigaki et al. \(2013\)](#) observed stars in thick disk and halo and found solar [Sr/Fe] ratios for $[\text{Fe}/\text{H}] \lesssim -1$.

3.1.2. Zirconium

Zirconium in Fig. 2b shows an increasing trend with decreasing metallicity, from [Zr/Fe] ≈ -0.1 at [Fe/H] ≈ 0.3 to [Zr/Fe] ≈ 0.3 for the most metal-poor stars in the sample at [Fe/H] ≈ -1 . [Borris et al. \(2000\)](#) found a [Zr/Fe] trend that seems to be only slightly super-solar with a large spread for stars with $[\text{Fe}/\text{H}] < -1.5$, and [Brewer & Carney \(2006\)](#) found basically solar [Zr/Fe] values for all their stars. The same was seen by [Reddy et al. \(2006\)](#) even if there seems to be a small trend from slight super-solar [Zr/Fe] at solar metallicity to slight sub-solar [Zr/Fe] for $[\text{Fe}/\text{H}] < -0.6$. On the other hand, the trend found by [Mashonkina et al. \(2007\)](#) is similar to what we find with an increasing trend from solar [Zr/Fe] value for solar metallicity stars to [Zr/Fe] ≈ 0.3 for $[\text{Fe}/\text{H}] \approx -1.5$. Recently [Mishenina et al. \(2013\)](#) observed F, G, and K dwarf stars in the Galactic disk finding a similar trend to ours even though the stars at super-solar metallicities show solar or slightly enhanced [Zr/Fe] values. Also [Ishigaki et al. \(2013\)](#) studied Zr finding a similar [Zr/Fe] trend

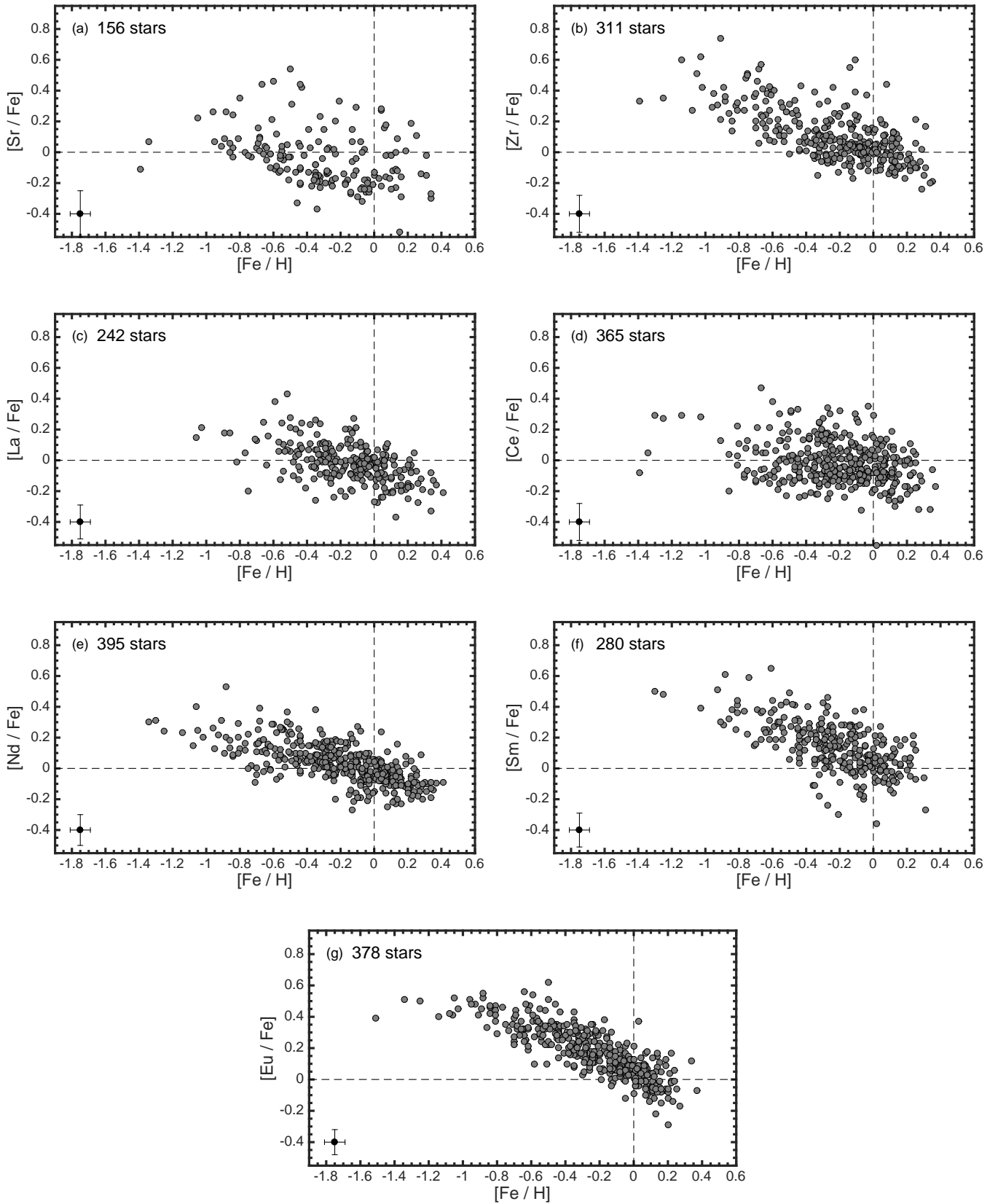


Fig. 2: Elemental abundance trends with Fe as the reference element. The number for stars for which the abundance has been derived is indicated in each plot.

Table 5: Comparisons of stellar parameters and abundances for stars in common to other studies. †

	Reddy03	Reddy06	Mashonkina04	Mashonkina07	Mishenina13
ΔT_{eff} [K]	132 ± 52 (13)	114 ± 114 (55)	4 ± 69 (19)	20 ± 101 (26)	-9 ± 54 (8)
$\Delta \log g$	0.05 ± 0.09 (13)	0.01 ± 0.17 (55)	0.01 ± 0.12 (19)	0.03 ± 0.13 (26)	0.04 ± 0.11 (8)
$\Delta[\text{Sr}/\text{H}]$	–	–	–	–	–
$\Delta[\text{Zr}/\text{H}]$	0.19 (1)	–	–	–0.02 (4)	0.08 (3)
$\Delta[\text{La}/\text{H}]$	–	–	–	–	0.18 (1)
$\Delta[\text{Ce}/\text{H}]$	0.23 (3)	–0.04 (14)	–	–0.18 (4)	0.12 (1)
$\Delta[\text{Nd}/\text{H}]$	0.16 (1)	–0.04 (15)	–0.12 (4)	–	0.12 (1)
$\Delta[\text{Sm}/\text{H}]$	–	–	–	–	0.21 (2)
$\Delta[\text{Eu}/\text{H}]$	–0.06 (1)	0.05 (21)	–	–	0.11 (2)

Notes. (†) Differences in stellar parameters from [Bensby et al. \(2014\)](#) and abundances from this work with the stars in common with [Reddy et al. \(2003, 2006\)](#), [Mashonkina et al. \(2004, 2007\)](#) and [Mishenina et al. \(2013\)](#). The differences are given as this work minus the other studies. In parenthesis, the number of common stars used for the different comparisons.

Table 6: Random errors in stellar parameters and abundances. †

Parameter	Random error (1- σ)
T_{eff}	51 K
$\log g$	0.07
[Fe/H]	0.05
ξ_1	0.08
[Sr/H]	0.15
[Zr/H]	0.12
[La/H]	0.11
[Ce/H]	0.12
[Nd/H]	0.10
[Sm/H]	0.11
[Eu/H]	0.08

Notes. (†) Mean standard errors for stellar parameters from [Bensby et al. \(2014\)](#). Errors for the neutron-capture elements are from this study.

to ours for their thick disk stars while for halo stars there is a decreasing trend to negative [Zr/Fe] values at low metallicities.

3.1.3. Lanthanum

As is shown in Fig. 2c, La presents mostly solar [La/Fe] values, with a possible trend from super-solar metallicity with [La/Fe] ≈ -0.3 to roughly solar [La/Fe] for [Fe/H] ≈ -0.6 . [Burris et al. \(2000\)](#) observed average solar [La/Fe] for [Fe/H] $\lesssim -1$ with increasing spread as metallicity decreases. [Simmerer et al. \(2004\)](#) derived abundances of La for giants and dwarfs in the metallicity range $-3 < [\text{Fe}/\text{H}] < 0.3$: for stars with the metallicity as in our sample, the agreement is good even if an offset of ~ 0.2 dex seems to be present. [Brewer & Carney \(2006\)](#) found a trend similar to what we found, with sub-solar [La/Fe] for solar metallicity stars that then increases to reach around solar [La/Fe] for [Fe/H] ≈ -0.6 . More recently [Mishenina et al. \(2013\)](#) found results in agreement with our trend as well as the thick disk sample of [Ishigaki et al. \(2013\)](#).

3.1.4. Cerium

In Fig. 2d Ce presents a basically flat and slightly sub-solar [Ce/Fe] abundance trend. This behaviour with [Ce/Fe] ≈ 0 is observed in [Reddy et al. \(2006\)](#) while a flat trend but slightly super-solar is found in [Brewer & Carney \(2006\)](#). However, in [Mashonkina et al. \(2007\)](#), the [Ce/Fe] trend is clearly increasing as metallicity decreases. Similar to our result is [Mishenina et al.](#)

(2013), where for solar metallicity and sub-solar metallicities, [Ce/Fe] shows a large spread around the solar [Ce/Fe] value.

3.1.5. Neodymium

Neodymium shows a tighter trend compared to the previous elements, as it is visible in Fig. 2e. The trend presents similarities to Zr, with sub-solar [Nd/Fe] for super-solar metallicity stars that then raises to [Nd/Fe] ≈ 0.2 at [Fe/H] ≈ -0.6 and for even lower metallicity the trend seems to be flat. [Burris et al. \(2000\)](#) presents a significant spread in [Nd/Fe], while [Mashonkina et al. \(2004\)](#) found a tight trend similar to what we found, with increasing [Nd/Fe] for decreasing metallicity up to [Nd/Fe] ≈ 0.3 for [Fe/H] ≈ -1 and then a plateau down to lower metallicity. The same general trend was found in [Brewer & Carney \(2006\)](#) while, on the other hand, the trend found in [Reddy et al. \(2006\)](#) is basically flat with [Nd/Fe] ≈ 0 . The result from [Mishenina et al. \(2013\)](#) is similar to ours, while [Ishigaki et al. \(2013\)](#) found flat trend with [Nd/Fe] = 0 for thick disk stars and [Nd/Fe] = 1 at [Fe/H] = -0.6 , that decrease to reach solar [Nd/Fe] for [Fe/H] -3 for halo stars.

3.1.6. Samarium

In Fig. 2f it is possible to distinguish a rising trend from solar [Sm/Fe] at solar metallicity up to [Sm/Fe] ≈ 0.5 at [Fe/H] ≈ -1 . Some of the previous listed works studied Sm as well. For example [Mishenina et al. \(2013\)](#) found a similar trend but with an offset of ≈ 0.2 dex, meaning that solar and super-solar metallicity stars have [Sm/Fe] ≈ -0.2 . Also [Ishigaki et al. \(2013\)](#) studied [Sm/Fe] finding basically solar value.

3.1.7. Europium

Europium (Fig. 2g) clearly shows a typical α -element trend, as is expected for an almost pure r-process element, since rapid neutron-capture is believed to happen in SN II. [Prochaska et al. \(2000\)](#) derived Eu abundances for four stars in metallicity range $-0.7 < [\text{Fe}/\text{H}] < -0.4$ showing high [Eu/Fe]. [Burris et al. \(2000\)](#) shows raising [Eu/Fe] as in [Mashonkina & Gehren \(2001\)](#) and [Koch & Edvardsson \(2002\)](#) where Eu shows a raising trend as we observed, with a steady increase from [Eu/Fe] ≈ -0.2 at [Fe/H] ≈ 0 up to [Eu/Fe] ≈ 0.4 for [Fe/H] ≈ -1.0 . A good agreement can be found in [Simmerer et al. \(2004\)](#), [Bensby et al. \(2005\)](#), [Brewer & Carney \(2006\)](#) and in [Reddy et al. \(2006\)](#) even if in this case the spread is higher. The same trend with

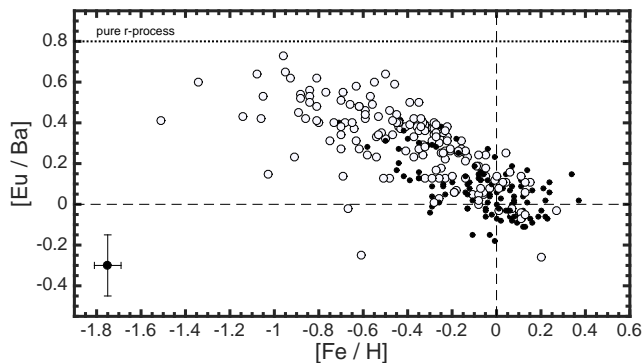


Fig. 3: $[\text{Eu}/\text{Ba}]$ as a function of $[\text{Fe}/\text{H}]$. The full sample is divided in thin and thick disk according to our age selection criterion. The dotted line represent pure r- process ratio derived from Bisterzo et al. (2014). The average error is also presented.

good agreement in values and shape is found in Mishenina et al. (2013) while in Ishigaki et al. (2013) the same trend is shifted to lower metallicity, as $[\text{Eu}/\text{Fe}] \approx 0$ for $[\text{Fe}/\text{H}] \approx -1$ and then $[\text{Eu}/\text{Fe}]$ raises to $+0.2$ at $[\text{Fe}/\text{H}] \approx -1.8$.

4. Origin of s- and r- elements

Most of the neutron-capture elements are produced from a mixture of r- and s-processes, and only in few cases only one of the two processes is the main responsible for the production. The comparison between such “prototype” elements of either the r- or the s-process, and other neutron-capture elements can help to constrain the production sites for the neutron-capture elements with uncertain origins. Barium, for instance, is often used in comparisons between neutron-capture elements due to its high s-process component. For example, Arlandini et al. (1999) derived the contributions of the s- and r-process to the solar Ba abundance being 81 % and 19 % respectively. However, since the work by Arlandini et al. (1999) several studies have been published with updated r- and s-process rates. For our comparisons we will use the values from Bisterzo et al. (2014).

The Ba abundances that we use in our study are derived with equivalent width from Bensby et al. (2014). Since Ba is known to suffer from NLTE for $T_{\text{eff}} > 6100$ (i.e. Korotin et al. 2011) and for this reason, in the comparisons with Ba we discarded the stars with high temperature. In Fig. 16 in Bensby et al. (2014) is visible the trend of $[\text{Ba}/\text{Fe}]$ as a function of $[\text{Fe}/\text{H}]$ together with the typical error on $[\text{Ba}/\text{Fe}]$ of about 0.1 dex. Once the stars with high temperature are removed, the $[\text{Ba}/\text{Fe}]$ trend is basically flat.

Several studies of the abundance structure in the Galactic disk have revealed the presence of two different stellar components that differ in age, kinematic and α -element abundances. The thin disk contains mostly young and kinematically cold stars with low α -abundance for a given metallicity while, on the other hand, the thick disk contains mostly old and kinematically hot stars with high α -abundance for given metallicity (Fuhrmann 1998; Bensby et al. 2003, 2005; Reddy et al. 2003, 2006; Adibekyan et al. 2012; Bensby et al. 2014). As suggested by Haywood et al. (2013) and Bensby et al. (2014), stellar ages seem to be a better separator between thin and thick disk stellar populations, than kinematic properties that largely overlap between the two. Following Bensby et al. (2014) we consider stars younger than 7 Gyr thin disk stars and stars older than 9 Gyr

thick disk stars. In all the following figures, if not specified otherwise, black dots are thin disk stars while white dots are thick disk stars as divided followed our criterion.

4.1. Eu

The comparison between Ba and Eu can be used as diagnostic of the neutron-capture process (Mashonkina & Gehren 2001) due to the different production of the two elements (Eu almost completely r-process, Ba mostly s-process). In Fig. 3 the $[\text{Eu}/\text{Ba}]$ ratio is close to the pure r-process line for metal-poor stars, meaning that the r-process was the only neutron-capture process active at the beginning of the formation of the Milky Way. As mentioned before, Eu is almost completely produced by the r-process, but Fig. 3 shows that also Ba was initially produced in this way, as already found for example by Burris et al. (2000). As soon as AGB stars start to be present and enrich the ISM with s-process elements, the $[\text{Eu}/\text{Ba}]$ ratio decreases until it reaches the solar value at solar metallicity. Comparing $[\text{Zr}/\text{Ba}]$ in Fig. 4 with $[\text{Eu}/\text{Ba}]$ it is possible to see that the rise in $[\text{Eu}/\text{Ba}]$ is steeper due to the almost complete production of Eu by r-process, meaning that as soon as enrichment from AGB stars become predominant, the $[\text{Eu}/\text{Ba}]$ ratio decreases quickly.

4.2. Sr and Zr

Barium can also be compared to Sr and Zr abundances to diagnose the processes that formed the Sr-Y-Zr peak elements (Travaglio et al. 2004). Figures 4a-b show the trends for $[\text{Sr}/\text{Ba}]$ and $[\text{Zr}/\text{Ba}]$ as a function of $[\text{Fe}/\text{H}]$. Even if the number of stars in the Sr case is lower than for Zr, the increases in $[\text{Sr}/\text{Ba}]$ and $[\text{Zr}/\text{Ba}]$ with decreasing metallicity are quite similar. Compared to $[\text{Eu}/\text{Ba}]$, $[\text{Zr}/\text{Ba}]$ shows a less steep rise with decreasing metallicity, probably because Zr has an higher s-process component than Eu. In addition to this, flat $[\text{Zr}/\text{Ba}]$ and $[\text{Sr}/\text{Ba}]$ trends are seen for stars around solar metallicity. Moreover, the abundances for thick disk stars at low-metallicity is particularly high, similar to what is visible in Fig. 3 for Eu, and is difficult to explain only with the $\approx 15\%$ and $\approx 20\%$ of r-production of Sr and Zr, respectively, from Arlandini et al. (1999). On the other hand, a shift of ≈ 0.2 dex is visible between $[\text{Sr}/\text{Ba}]$ and $[\text{Zr}/\text{Ba}]$.

Travaglio et al. (2004) compared their galactic chemical evolution model with observations down to $[\text{Fe}/\text{H}] \approx -4$. The model consists of Sr produced of 71 % from low-intermediate mass AGB stars ($1-8 M_{\odot}$) defined as *main* s-process, and for 9 % from advanced evolution phases of massive stars defined as *weak* s-process. For Zr they derive 65 % *main* s-process contribution and an almost negligible contribution from the *weak* s-process of about 2 %. From their results, Travaglio et al. (2004) claim an r-process contribution of $\approx 20\%$ and $\approx 30\%$ that is higher than what derived by Arlandini et al. (1999). However, in their comparison with r-process rich and very metal-poor stars, they derive that pure r-process production for Sr and Zr is $\approx 10\%$ (more precisely 12 % for Sr and 15 % for Zr). Summing up the last derived r-contribution with the s- contribution mentioned above, it can be noticed that 8 % of Sr and 18 % of Zr is missing and it is of “primary” origin from massive stars at low metallicity. Unfortunately the real process for this LEPP (lighter element primary process) is still not clear because detailed supernovae model calculations for massive stars at low metallicity are still not available (Travaglio et al. 2004). More recently, Bisterzo et al. (2014) re-calculated the contribution for Sr and Zr, and found similar results as Travaglio et al. (2004), still requiring LEPP as well.

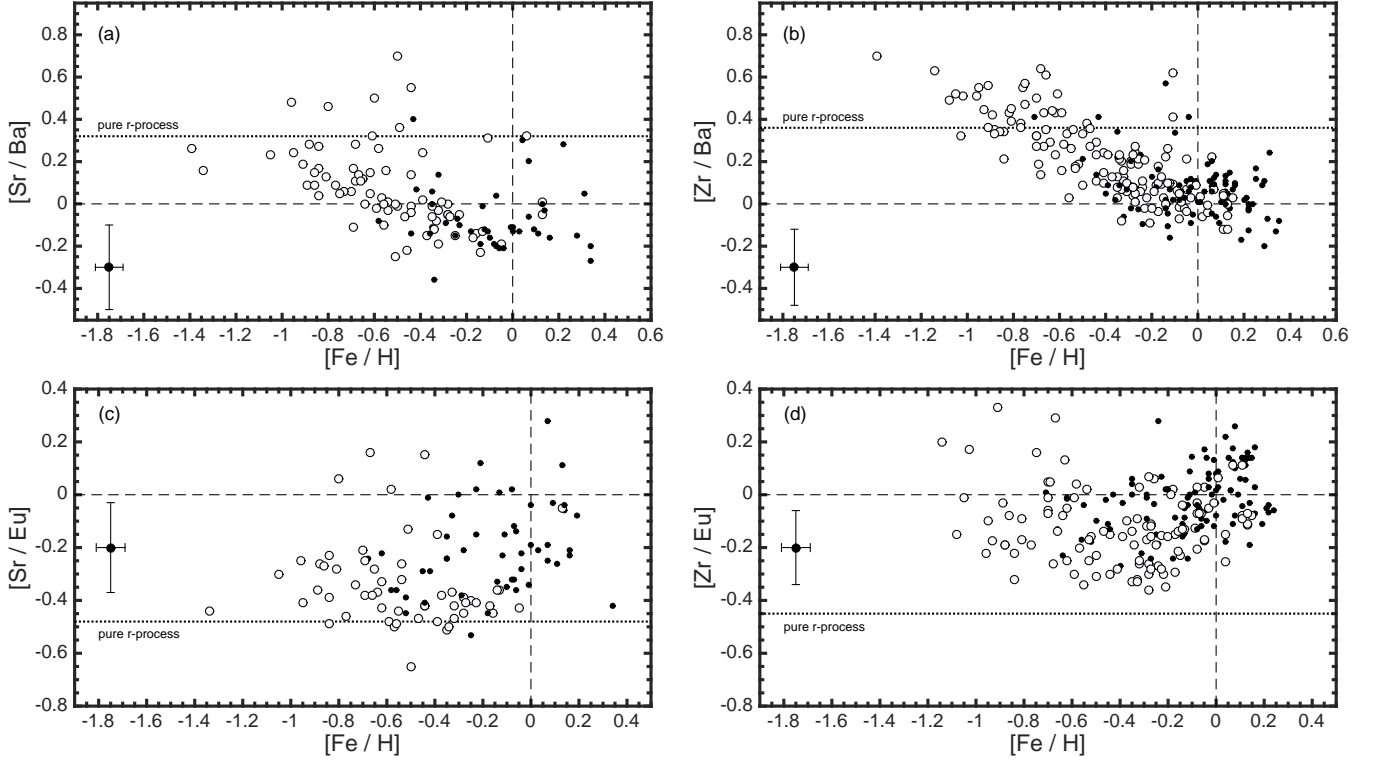


Fig. 4: $[\text{Sr}/\text{Ba}]$ (panel (a)), $[\text{Zr}/\text{Ba}]$ (panel (b)) as a function of $[\text{Fe}/\text{H}]$ and $[\text{Sr}/\text{Eu}]$ (panel (c)) and $[\text{Zr}/\text{Eu}]$ (panel (d)) as a function of $[\text{Fe}/\text{H}]$. The full sample is divided in thin and thick disk according to our age selection criterion. The dotted line represent pure r-process ratio derived from [Bisterzo et al. \(2014\)](#). The average error is also indicated.

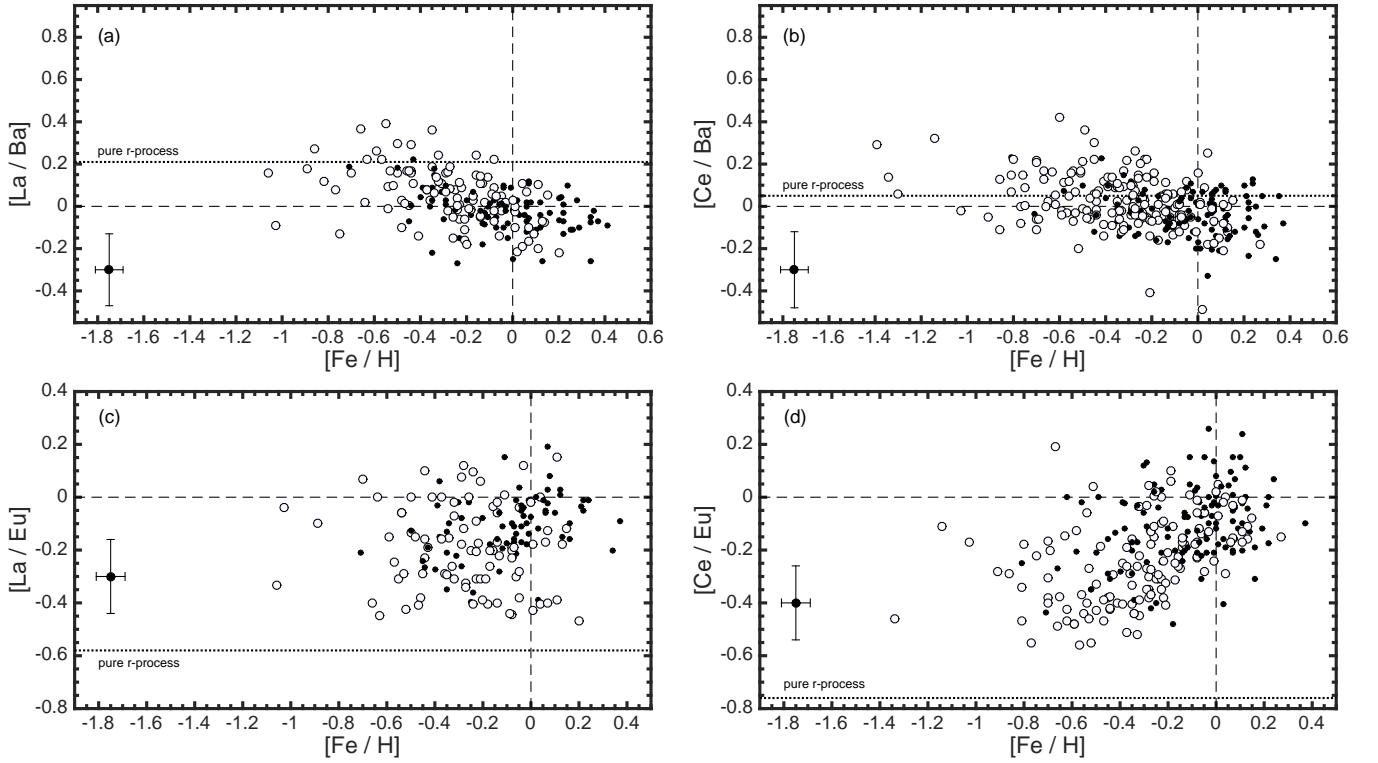


Fig. 5: $[\text{La}/\text{Ba}]$ and $[\text{Ce}/\text{Ba}]$ (panels (a) and (b) respectively) and $[\text{La}/\text{Eu}]$ and $[\text{Ce}/\text{Eu}]$ (panels (c) and (d) respectively) as a function of $[\text{Fe}/\text{H}]$. The full sample is divided in thin and thick disk according to our age selection criterion. The dotted line represent pure r-process ratio derived from [Bisterzo et al. \(2014\)](#). The average error is also indicated.

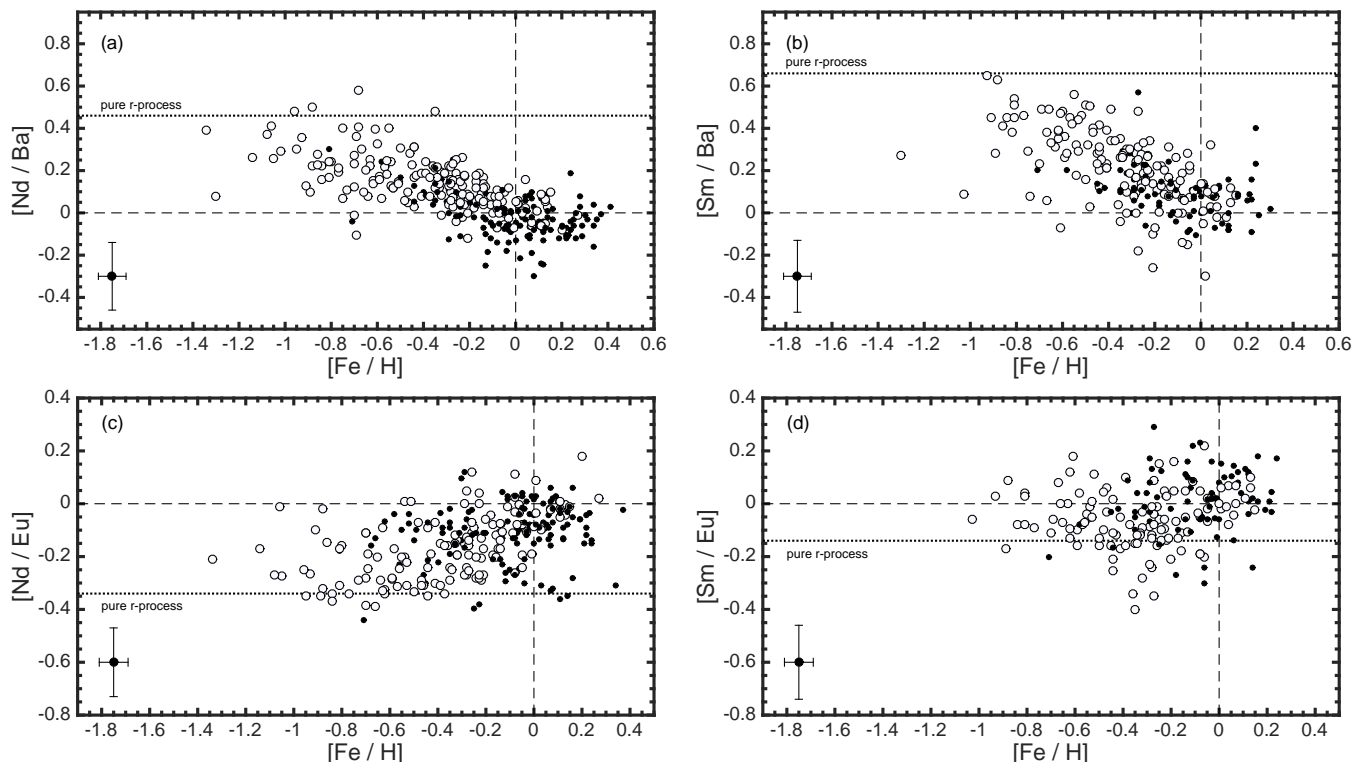


Fig. 6: $[\text{Nd}/\text{Ba}]$ and $[\text{Sm}/\text{Ba}]$ (panels (a) and (b) respectively) and $[\text{Nd}/\text{Eu}]$ and $[\text{Sm}/\text{Eu}]$ (panels (c) and (d) respectively) as a function of $[\text{Fe}/\text{H}]$. The full sample is divided in thin and thick disk according to our age selection criterion. The dotted line represent pure r-process ratio derived from [Bisterzo et al. \(2014\)](#). The average error is also indicated.

The different LEPP contribution for Sr and Zr could be the explanation of the ≈ 0.2 dex between Sr and Zr, where the higher plateau of $[\text{Zr}/\text{Ba}]$ could be explained with the higher contribution from LEPP, i.e. more enrichment of Zr from high massive stars at low metallicity.

The comparison with the [Travaglio et al. \(2004\)](#) model, however, is unable to match our data since it predicts a solar $[\text{Sr}/\text{Ba}]$ and $[\text{Zr}/\text{Ba}]$ down to $[\text{Fe}/\text{H}] \approx -1$. A possible explanation for this discrepancy can come from the large uncertainties that still exist for the yields of heavy elements from AGB stars due to missing models for stars in the range $1-8 M_{\odot}$ at different metallicities ([Karakas 2014](#)).

4.3. La, Ce, Nd and Sm

Figures 5a-d show $[\text{La}/\text{Ba}]$, $[\text{Ce}/\text{Ba}]$, $[\text{La}/\text{Eu}]$, and $[\text{Ce}/\text{Eu}]$ versus $[\text{Fe}/\text{H}]$. La and Ce are part of the second peak of the magic neutron number 82 together with Sm and Eu. From Fig. 2c and Fig. 2d La and Ce do not show any particular trend with metallicity and this is also reflected in the upper panels of Figs. 5. In the lower panels of Fig. 5, $[\text{La}/\text{Eu}]$ and $[\text{Ce}/\text{Eu}]$ are plotted over $[\text{Fe}/\text{H}]$ to evaluate their small r-process enrichment branch and the trends look similar. Compared to Sr and Zr, for example, it is possible to see that the increases in $[\text{La}/\text{Eu}]$ and $[\text{Ce}/\text{Eu}]$ are fast and happens when AGB stars start to contribute. From Fig. 5d it is visible a change in slope at $[\text{Fe}/\text{H}] \approx -0.5$. This could be the moment where the enrichment of ISM from AGB stars start to dominate, represented as a steady increase in $[\text{Ce}/\text{Eu}]$ as $[\text{Fe}/\text{H}]$ increases toward solar values.

A similar investigation was performed for Nd that is produced in almost equal parts by s- and r-processes. In both pan-

els of Fig. 6, Nd shows smooth trends, with high Nd abundance for metal-poor stars that decreases as metallicity increases. Interestingly the most metal-poor stars in both panels are close to the theoretical abundance ratio for r-process derived using [Bisterzo et al. \(2014\)](#) values. Very similar results are derived in Nd work by [Mashonkina et al. \(2004\)](#). The decrease that is present in $[\text{Nd}/\text{Ba}]$ is due to the higher rate of s-production of Ba compared to Nd (81 % for Ba and 56 % for Nd), while the decrease in $[\text{Nd}/\text{Eu}]$ is produced by the higher rate (93 %) of r-production for Eu compared to Nd. Similar results can be found for Sm due to its high percentage of r-process production. In Fig. 6a, thin disk stars have on average smaller $[\text{Nd}/\text{Ba}]$ compared to thick disk stars, and are more concentrated along solar $[\text{Nd}/\text{Ba}]$ values. This means that during thick disk formation and evolution, the r-process contribution was higher than in the thin disk, probably because the thick disk formed in a rapid way with high star formation rate that produced more massive stars responsible for r-process enrichment.

We also investigated $[\text{Sm}/\text{Ba}]$ and $[\text{Sm}/\text{Eu}]$ versus $[\text{Fe}/\text{H}]$ and the results can be seen in Figs. 6b and d. From Fig. 6b it is clear that the most metal-poor stars in our sample are close to the pure solar r-process meaning that r-process was the main active channel for the production of Sm. This is expected, considering that Sm is produced for almost 70 % via rapid neutron-capture. Since Eu is an r-process, it is interesting to investigate $[\text{Sm}/\text{Eu}]$ (Fig. 6d). The high percentage of production via rapid neutron-capture for both Sm and Eu, is responsible for the $[\text{Sm}/\text{Eu}] \approx 0$ until solar metallicity. For super-solar metallicity, $[\text{Sm}/\text{Eu}]$ seems to be on average higher than solar value, probably because at this metallicities regime the s-process production of Sm is more important.

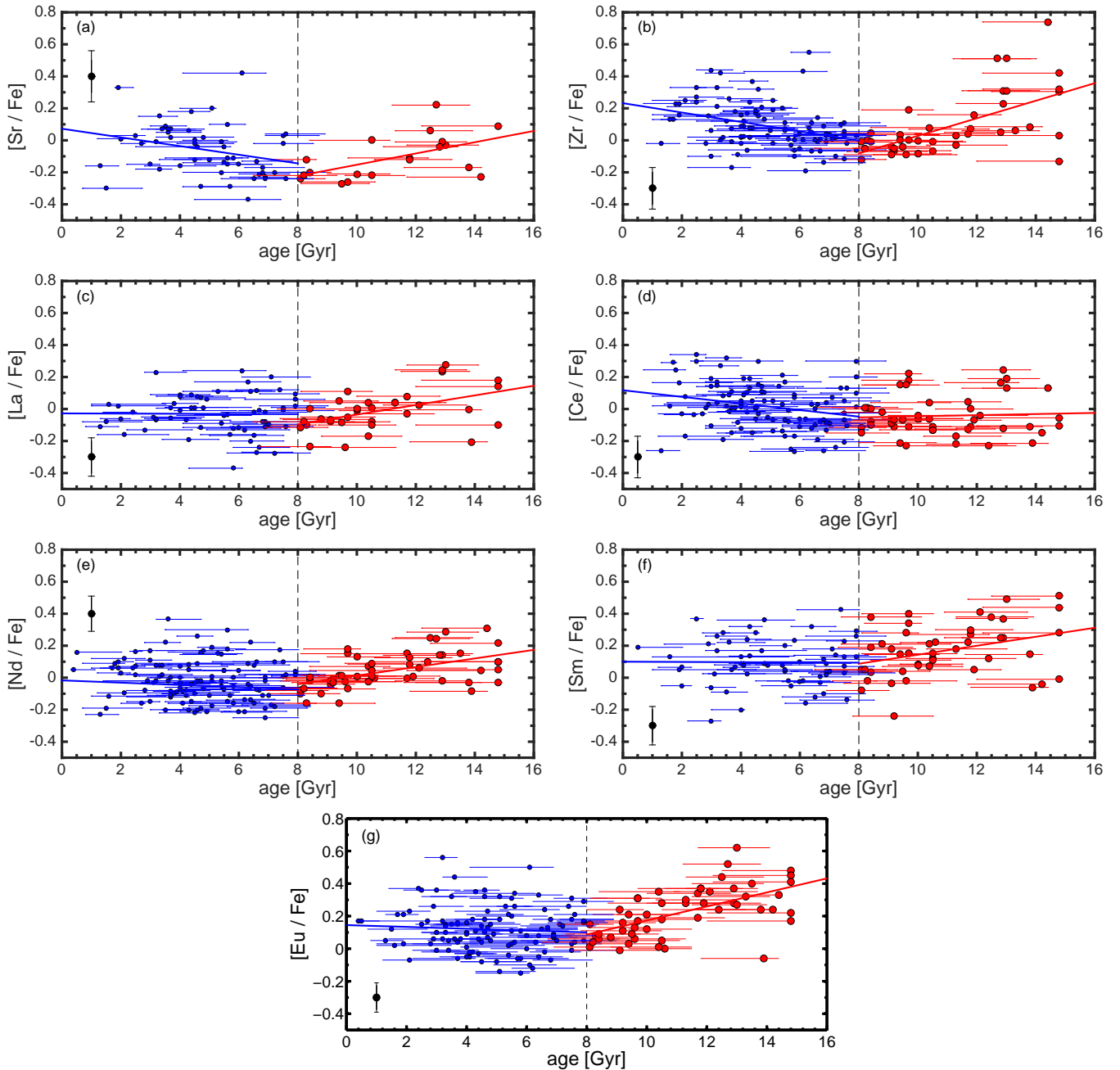


Fig. 7: $[X/Fe]$ for neutron-capture elements compared to age. Only stars with age uncertainties less than 3 Gyr are plotted. The vertical dot line at 8 Gyr indicate an approximate age separation between thin and thick disk. Blue dots represent young thin disk stars while red dots are for old thick disk stars. The blue and red lines indicate the best fit for thin and thick disk stars. The errors on the ages are from [Bensby et al. \(2014\)](#). The average error on the abundance ratio is indicated in black.

The formation of the elements La, Ce, Nd and Eu was studied by [Travaglio et al. \(1999\)](#) and it is interesting since these elements are part of the magic neutron number $N = 82$. [Travaglio et al. \(1999\)](#) found that the main s-process contribution to these elements come from AGB stars in the range $2-4 M_{\odot}$ while the r-process contribution is mainly due to stars in the range $8-10 M_{\odot}$. In their calculation, AGB contribution starts to be important for $[Fe/H] \gtrsim -1.5$, meaning that after this point, the Eu abundance decreases while the abundances for the other elements increase, especially for Ce and La because of their larger s-process contribution.

The models of [Travaglio et al. \(1999\)](#) are in agreement with our data, as can be seen comparing our Figs. 2c, d, e, f with their Figs. 7, 8, 10, and 11. Their model of Eu enrichment is in agreement with what we found in Fig. 2g and it can be explained by r-process derived from SN II from $8-10 M_{\odot}$ stars.

5. Abundance evolution with age

Since the r- and s-processes happen at different timescale in Galactic evolution, we now investigate how the $[X/Fe]$ abundance ratios vary with time. Only stars with stellar ages with

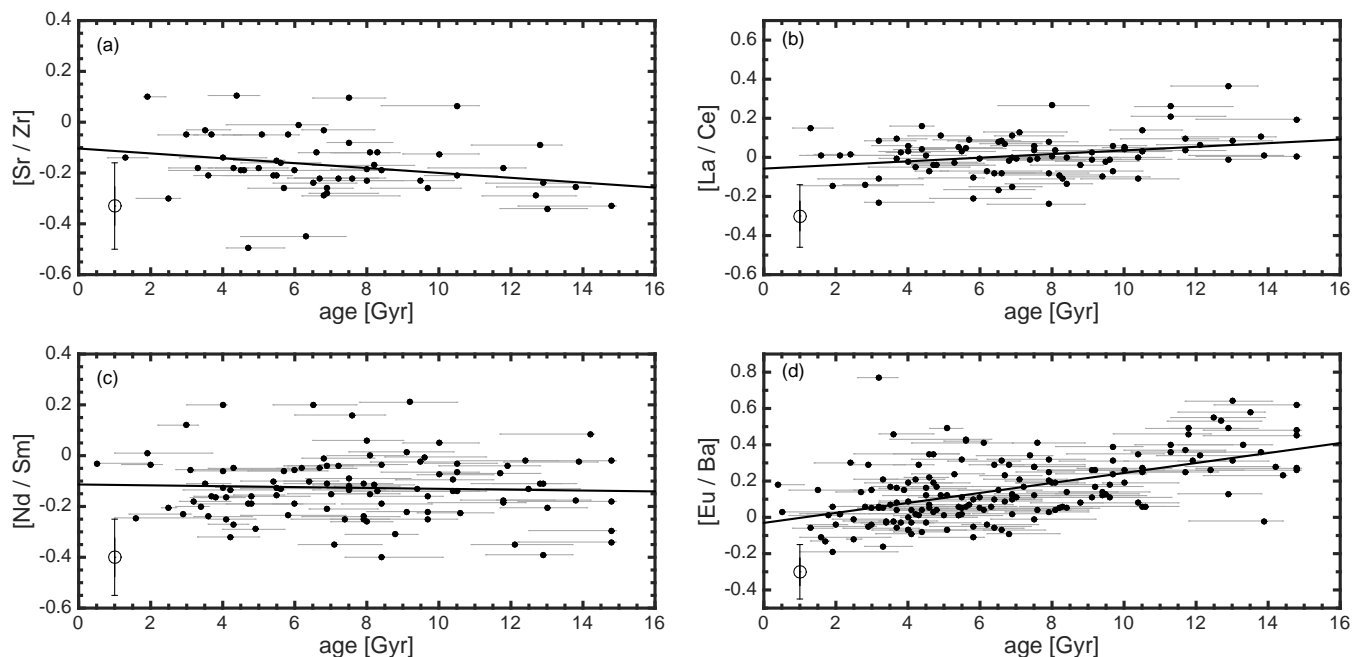


Fig. 8: $[\text{Sr}/\text{Zr}]$, $[\text{La}/\text{Ce}]$, $[\text{Nd}/\text{Sm}]$ and $[\text{Eu}/\text{Ba}]$ compared to age. Only stars with age uncertainties less than 3 Gyr are plotted. The black line in each plot represent the best fit. The errors on the ages are taken from [Bensby et al. \(2014\)](#). The average error on the abundance ratio is indicated in the lower left part of each plot.

uncertainties less than 3 Gyr are used (derived as the maximum age estimation minus the minimum one). As before, stars with ages less than 7 Gyr are considered to be part of the thin disk, while stars older than 9 Gyr are part of the thick disk. We stress here that the stellar ages are really accurate in relative terms, meaning that the relative age differences between stars is good.

The results are presented in Fig. 7. The first thing that can be noticed is that in most of the cases there is a change in the slopes at an age of about 8 Gyr, which happens coincide with the interface between the thin and thick disks. For the thick disk (stars older than 8 Gyr) the indication that we get from Fig. 7 is that enrichment of neutron-capture elements was higher at the early times of the Milky Way, so the r-process could produce large quantities of neutron-capture elements, even if only thanks to stars with masses in the 8-10 M_{\odot} range. This could be explained assuming an intense and rapid star formation in the process of building up of the thick disk that ended around 8 Gyr ago. The decrease is then due to a reduction of r-process production with at the same time the beginning of s-process production. The basically flat $[X/\text{Fe}]$ in thin disk for La, Ce, Nd, Sm and Eu can be explained as a combination of the fact that the contribution from low- and intermediate mass stars in AGB phase become more important, but this contribution is similar to Fe production from SN Ia, meaning a flattening in the ratio. In addition to this, since the s-process in the AGB phase requires seed nuclei of iron-group elements, the increase in metallicity of younger stars would produce an increase in the yields of neutron-capture elements.

Interestingly, for Sr and Zr we see in Fig. 7a and Fig. 7b that abundances increase for younger thin disk stars. This phenomenon can be explained, as before, by the fact that the s-process is the main responsible for enrichment in thin disk, but with the addition that these two elements present the highest s-process rate among the other neutron-capture elements in this

study (70% for Sr and 65% for Zr, as derived by [Bisterzo et al. 2014](#)). Unfortunately, at this moment we cannot explain the high spread in $[\text{Zr}/\text{Fe}]$ for the very old stars.

Considering the results in Figs. 4, 5, and 6, neutron-capture elements can be paired as they seem to share similar properties. For this reason we investigate how the abundance ratios of these element pairs change at different ages. The results are shown in Fig. 8, with the addition of the $[\text{Eu}/\text{Ba}]$ ratio.

As expected for elements that share the same production sites, the trends are almost flat, within the uncertainties. For $[\text{Sr}/\text{Zr}]$ in Fig. 8a, there are indications for higher Zr production at early stage than Sr. A possible explanation could be that Zr is claimed to have an higher r-process production (15% from classical r-process plus 18% from LEPP, [Travaglio et al. 2004](#)) that will produce more Zr in the early stages of the evolution of the Galaxy. The $[\text{La}/\text{Ce}]$ ratio in Fig. 8b presents a flat trend, indicating shared sites and mechanisms of production. For $[\text{Nd}/\text{Sm}]$ in Fig. 8c the trend is basically flat, also in this case indicating shared production sites.

The trend of $[\text{Eu}/\text{Ba}]$ can be explained in a different way. Eu and Ba have clearly different histories of productions and here are paired because they are typical representatives of the r- and s-processes, respectively. In Fig. 8d the decrease of $[\text{Eu}/\text{Ba}]$ towards younger ages can be explained as an increase in production of Ba and a simultaneous decrease in Eu because AGB stars become more important than SN II after about 1 Gyr from the bulk of star formation.

We also investigate the trends of $[X/\text{H}]$ with respect to age. This kind of investigation is not present in previous works since the age determination was not good enough. Results are presented in Fig. 9, using the same color coding as in Fig. 7, with stars with an age greater than 9 Gyr considered as thick disk and stars younger than 7 Gyr thin disk.

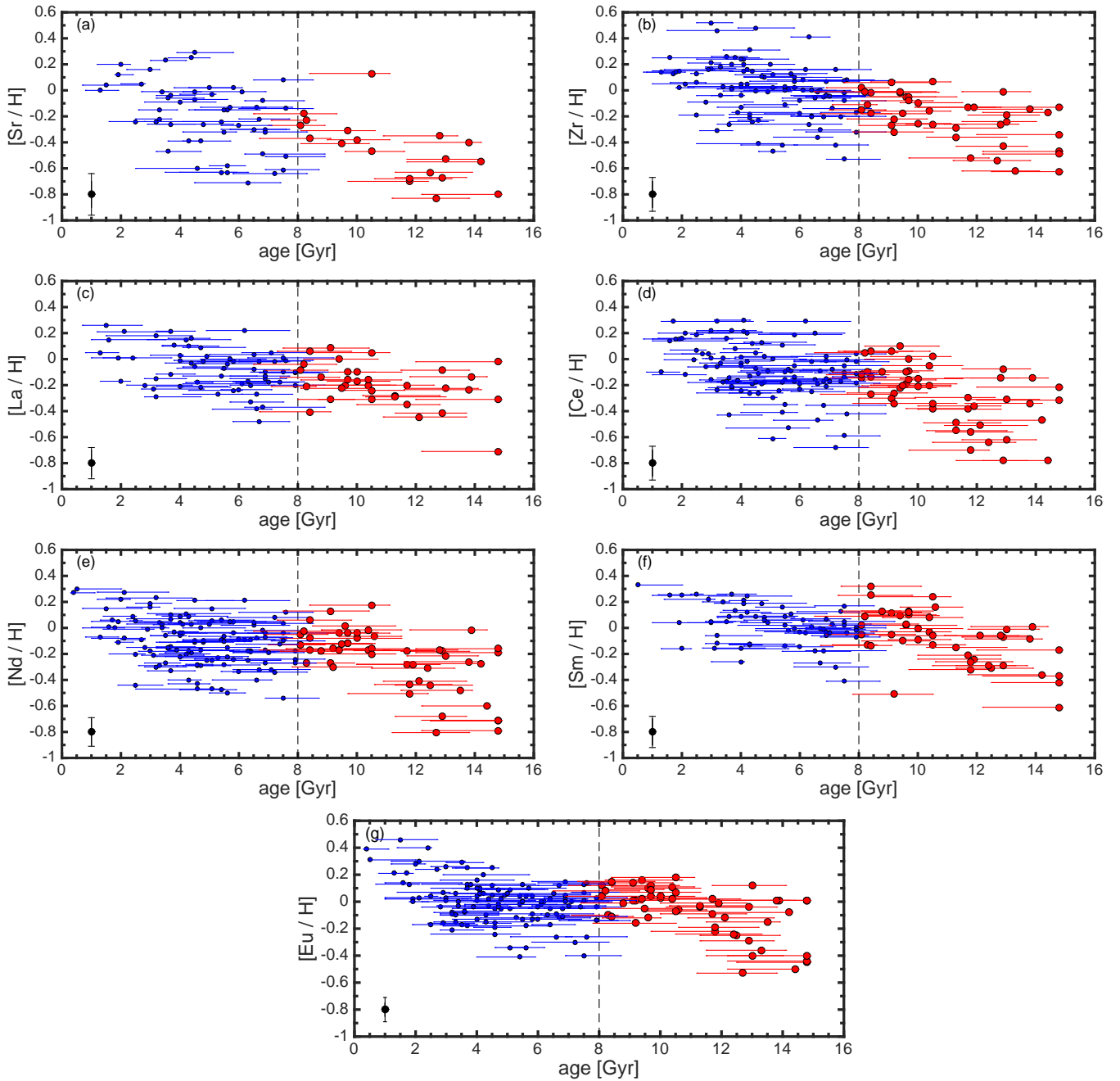


Fig. 9: $[X/H]$ for neutron-capture elements compared to age. Only stars with age uncertainties less than 3 Gyr are plotted. The vertical dot line at 8 Gyr indicate an approximate age separation between thin and thick disk. Blue dots represent young thin disk stars while red dots are for old thick disk stars. The errors on the ages are from [Bensby et al. \(2014\)](#). The average error on the abundance ratio is indicated in black.

It is possible to see that in all the elements, apart for Sr probably due to the big scatter and the lower number of stars with a successful analysis, the trend is really similar. We checked for possible correlations with stellar parameters that could explain the trend in Fig. 9 finding none.

From older ages there is a steep increase that ends at 11 Gyr, that is probably due to the production of these elements via SN II. This rise is then followed by a more flat part that in some cases ends in a increase in $[X/H]$ for younger stars. This final increase can be explained considering the contribution from low-

mass stars that polluted the gas from where the youngest stars were formed. However in the case of $[Eu/H]$, this explanation has more problem to explain the results because Eu is almost completely produced via r-process meaning that the contribution from low-mass stars should be almost negligible.

In Fig. 15 in [Bensby et al. \(2014\)](#), it is possible to see the different abundance trends for different α -elements. In particular Ti shows a clearer distinction between thin and thick disk compared to the other α -elements, so we decided to use Ti to distinguish thin and thick disk stars in the $[X/H]$ versus age comparison. We

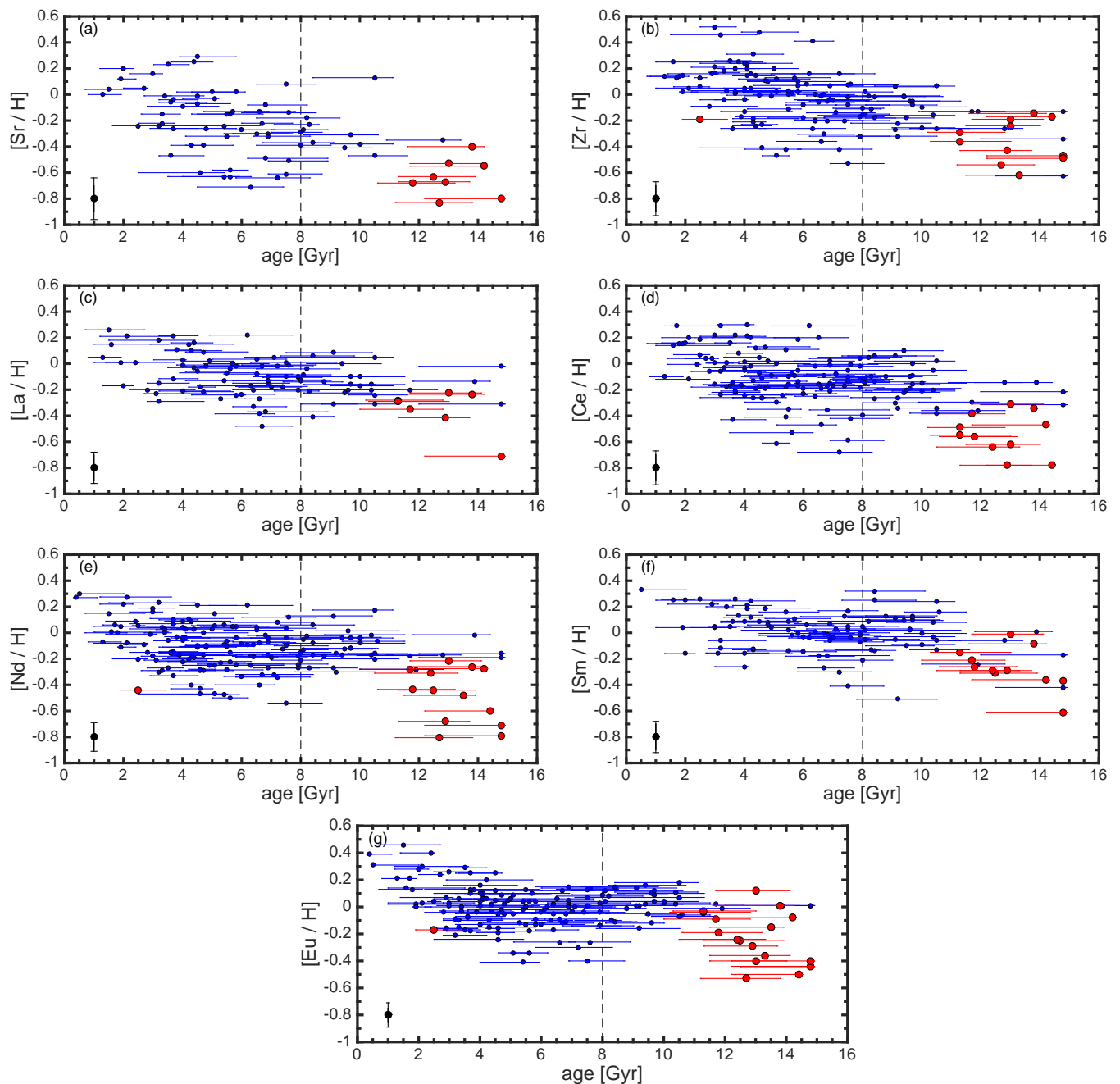


Fig. 10: $[X/H]$ for neutron-capture elements compared to age. Only stars with age uncertainties less than 3 Gyr are plotted. The vertical dot line at 8 Gyr indicate an approximate age separation between thin and thick disk. Blue dots represent thin disk stars with $[Ti/Fe] < 0.2$ while red dots are for thick disk stars identified with $[Ti/Fe] > 0.2$. The average error on the abundance ratio is indicated in black.

consider stars being thin disk stars when $[Ti/Fe] < 0.2$, while stars are thick disk stars when $[Ti/Fe] > 0.2$. The results are visible in Fig. 10 for all the elements under investigation. Clearly basically all thick disk stars are located in the old age region and are responsible for the increase that is visible in Fig. 9 up to 11 Gyr. All thin disk stars are instead responsible for the flat and the uprising part at young age.

6. Summary

We have performed a detailed chemical abundance analysis on a sample of F and G dwarf stars for several neutron-capture elements Sr, Zr, La, Ce, Nd, Sm and Eu in order to investigate their formation sites and their evolution in the Galactic disk. In the literature there are several works that focus on metal-poor stars due to their interesting highly enriched spectra, while for stars with $[Fe/H] > -1$ the samples are usually smaller and not all the elements can be investigated due to the spectra that become extremely rich. In total we determine Sr abundance for 156 stars,

Zr abundance for 311 stars, La abundance for 242 stars, Ce abundance for 365 stars, Nd abundance for 395 stars, Sm abundance for 280 stars and Eu abundance for 378 stars. In summary our findings and conclusions are:

- Strontium and zirconium are part of the same s-process peak production and they are intensively studied in theoretical works due to their position in the valley of stability due to the magic neutron number $A = 50$. They show similar abundance trends with a common flat part around solar metallicity. For Sr, the spread in thin and thick disk is too high to derive any conclusion. For Zr instead, the thin disk stars are grouped close to solar abundance values meaning a constant production in time, thanks to production in AGB stars in the mass range $1-8 M_{\odot}$. Models from Travaglio et al. (2004) cannot explain our Sr trend since it is expected to be basically flat around solar $[\text{Sr}/\text{Fe}]$ down to $[\text{Fe}/\text{H}] \approx -2$. On the other hand, the same models can fit our Zr data, even if we observe sub-solar $[\text{Zr}/\text{Fe}]$ at solar metallicity. The discrepancies could be due to uncertainties in the model on yields for stars in $1-8 M_{\odot}$ range at different metallicities.
- Lanthanum and cerium are basically flat, with solar $[\text{La}, \text{Ce}/\text{Fe}]$. This flat trend at solar value is basically conserved also when La and Ce are compared to Ba, a typical s-process element. When compared to Eu, some thick disk stars show pure r-process abundance and it is possible to see a turn in $[\text{Ce}/\text{Eu}]$ when s-process become the more important enrichment process at $[\text{Fe}/\text{H}] \approx -0.5$. In Travaglio et al. (1999), r-process La and Ce productions come from SN II from stars of $8-10 M_{\odot}$, while s-process production come from stars in the range $2-4 M_{\odot}$. This gives a gap in the production of La and Ce and then a fast decrease as soon as AGB stars are actively involved in chemical enrichment, since Eu is basically not produce via this channel.
- Neodymium and samarium are produced via both the s- and r-processes. For Nd the two processes are almost equally responsible for its enrichment while for Sm r-process is the main productive channel (70%). Even if they are produced in different ways they share a similar trend as α -element, derived by production from SN II. Considering the results from Travaglio et al. (1999) on different AGB sites for Nd, Sm and Ba, the smooth decrease in $[\text{Nd}/\text{Ba}]$ is due to the fact that Nd has a quite high r-process production rate compared to Ba but at solar metallicities the flat $[\text{Nd}/\text{Ba}]$ is due to the common production from stars in the mass range $2-4 M_{\odot}$. Samarium, on the other hand, has a higher r-process production rate that makes it more similar to Eu, so $[\text{Sm}/\text{Eu}]$ is almost flat with values around $[\text{Sm}/\text{Eu}] = 0$.
- Europium is the prototype of r-process element since its production is almost completely performed by rapid neutron-capture. It shows a really clean α -trend when compared to metallicity, as Nd and Sm. This is expected since its high r-process production rate and both thin and thick disk stars present the same $[\text{Eu}/\text{Ba}]$ decrease. Our data are in agreement with model from Travaglio et al. (1999) considering enrichment from SN II of mass $8-10 M_{\odot}$.
- The study of abundances as function of age shows different trend for thin and thick disk in almost all the elements. This is especially true for Sr, Zr, Nd, and Eu. In thick disk there is a decrease in the abundance as age decreases that can be explained with the decrease of SN II events while Fe production from SN Ia increases. In the thin disk most of the trends are basically flat because of the high production of neutron-capture elements via s-process from AGB stars. This is not

the case for Sr and Zr that show increasing abundances for younger stars due to the high s-production rate, as derived by Bisterzo et al. (2014). $[\text{Sr}/\text{Zr}]$ shows an increasing trend with decreasing ages, probably due to higher Zr r- process production. The same production sites produce flat $[\text{La}/\text{Ce}]$ and $[\text{Nd}/\text{Sm}]$. When $[\text{Eu}/\text{Ba}]$ is related to age the trend shows a decrease with lower ages, due to the decrease in Eu production by SN II counterbalance by the increase in production by AGB stars of Ba.

When the $[X/\text{H}]$ ratio is plotted as a function of the age, it is clear that around 11 Gyr the trend changes clearly in almost all the elements, showing a flatter trend after a rise from older ages up to 6 Gyr, followed in some cases by a clear increase in $[X/\text{H}]$ at recent age. This is particularly relevant in Eu case, and the reason is not completely clear. In theory younger stars should not present such high abundance in Eu, since Eu is almost completely produced in SN II at the beginning of star formation. In theory if these stars are coming from an inner region of the Galaxy where the metallicity is higher compared to the Solar Neighborhood, the higher $[\text{Eu}/\text{H}]$ also at younger stellar ages could be potentially explained. This possible explanation needs however to be studied in more detailed, taking into account also the orbit of the stars and possible membership with dynamical streams (for example Hercules streams, since it was studied in Bensby et al. (2014)).

Acknowledgements

We would like to thank the referee Prof. Chris Sneden for the useful comments and suggestions in the improvement of this paper. T.B. was supported by the project grant "The New Milky Way" from the Knut and Alice Wallenberg Foundation.

References

- Adibekyan, V. Z., Sousa, S. G., Santos, N. C., et al. 2012, *A&A*, 545, A32
 Andrievsky, S. M., Spite, F., Korotin, S. A., et al. 2011, *A&A*, 530, A105
 Aoki, W., Ryan, S. G., Norris, J. E., et al. 2001, *ApJ*, 561, 346
 Arlandini, C., Käppeler, F., Wisshak, K., et al. 1999, *ApJ*, 525, 886
 Asplund, M., Grevesse, N., Sauval, A. J., & Scott, P. 2009, *ARA&A*, 47, 481
 Battistini, C. & Bensby, T. 2015, *A&A*, 577, A9
 Bautista, M. A., Gull, T. R., Ishibashi, K., Hartman, H., & Davidson, K. 2002, *MNRAS*, 331, 875
 Bedell, M., Meléndez, J., Bean, J. L., et al. 2014, *ApJ*, 795, 23
 Bensby, T., Feltzing, S., & Lundström, I. 2003, *A&A*, 410, 527
 Bensby, T., Feltzing, S., Lundström, I., & Ilyin, I. 2005, *A&A*, 433, 185
 Bensby, T., Feltzing, S., & Oey, M. S. 2014, *A&A*, 562, A71
 Bisterzo, S., Gallino, R., Straniero, O., Cristallo, S., & Käppeler, F. 2011, *MNRAS*, 418, 284
 Bisterzo, S., Travaglio, C., Gallino, R., Wiescher, M., & Käppeler, F. 2014, *ApJ*, 787, 10
 Brewer, M.-M. & Carney, B. W. 2006, *AJ*, 131, 431
 Burbidge, E. M., Burbidge, G. R., Fowler, W. A., & Hoyle, F. 1957, *Reviews of Modern Physics*, 29, 547
 Burris, D. L., Pilachowski, C. A., Armandroff, T. E., et al. 2000, *ApJ*, 544, 302
 Cescutti, G., François, P., Matteucci, F., Cayrel, R., & Spite, M. 2006, *A&A*, 448, 557
 Demarque, P., Woo, J.-H., Kim, Y.-C., & Yi, S. K. 2004, *ApJS*, 155, 667
 Frebel, A. & Norris, J. E. 2013, *Metal-Poor Stars and the Chemical Enrichment of the Universe*, ed. T. D. Oswalt & G. Gilmore, 55
 Freeman, K. & Bland-Hawthorn, J. 2002, *ARA&A*, 40, 487
 Freiburghaus, C., Rosswog, S., & Thielemann, F.-K. 1999, *ApJ*, 525, L121
 Fuhrmann, K. 1998, *A&A*, 338, 161
 Gustafsson, B., Edvardsson, B., Eriksson, K., et al. 2008, *A&A*, 486, 951
 Haywood, M., Di Matteo, P., Lehnert, M. D., Katz, D., & Gómez, A. 2013, *A&A*, 560, A109
 Ishigaki, M. N., Aoki, W., & Chiba, M. 2013, *ApJ*, 771, 67
 Ivans, I. I., Simmerer, J., Sneden, C., et al. 2006, *ApJ*, 645, 613

- Karakas, A. I. 2014, in IAU Symposium, Vol. 298, IAU Symposium, ed. S. Feltzing, G. Zhao, N. A. Walton, & P. Whitelock, 142–153
- Koch, A. & Edvardsson, B. 2002, A&A, 381, 500
- Korotin, S., Mishenina, T., Gorbaneva, T., & Soubiran, C. 2011, MNRAS, 415, 2093
- Kupka, F., Piskunov, N., Ryabchikova, T. A., Stempels, H. C., & Weiss, W. W. 1999, A&AS, 138, 119
- Kupka, F. G., Ryabchikova, T. A., Piskunov, N. E., Stempels, H. C., & Weiss, W. W. 2000, Baltic Astronomy, 9, 590
- Lambert, D. L. 1989, in American Institute of Physics Conference Series, Vol. 183, Cosmic Abundances of Matter, ed. C. J. Waddington, 168–199
- Lawler, J. E., Den Hartog, E. A., Sneden, C., & Cowan, J. J. 2006, ApJS, 162, 227
- Lawler, J. E., Sneden, C., Cowan, J. J., Ivans, I. I., & Den Hartog, E. A. 2009, ApJS, 182, 51
- Lawler, J. E., Wickliffe, M. E., den Hartog, E. A., & Sneden, C. 2001, ApJ, 563, 1075
- Ljung, G., Nilsson, H., Asplund, M., & Johansson, S. 2006, A&A, 456, 1181
- Mashonkina, L. & Gehren, T. 2001, A&A, 376, 232
- Mashonkina, L. I., Kamaeva, L. A., Samotoev, V. A., & Sakhbullin, N. A. 2004, Astronomy Reports, 48, 185
- Mashonkina, L. I., Vinogradova, A. B., Ptitsyn, D. A., Khokhlova, V. S., & Chernetsova, T. A. 2007, Astronomy Reports, 51, 903
- Mishenina, T. V., Pignatari, M., Korotin, S. A., et al. 2013, A&A, 552, A128
- Nishimura, S., Kotake, K., Hashimoto, M.-a., et al. 2006, ApJ, 642, 410
- Pignatari, M., Gallino, R., Heil, M., et al. 2010, ApJ, 710, 1557
- Piskunov, N. E., Kupka, F., Ryabchikova, T. A., Weiss, W. W., & Jeffery, C. S. 1995, A&AS, 112, 525
- Prochaska, J. X., Naumov, S. O., Carney, B. W., McWilliam, A., & Wolfe, A. M. 2000, AJ, 120, 2513
- Reddy, B. E., Lambert, D. L., & Allende Prieto, C. 2006, MNRAS, 367, 1329
- Reddy, B. E., Tomkin, J., Lambert, D. L., & Allende Prieto, C. 2003, MNRAS, 340, 304
- Roederer, I. U., Lawler, J. E., Sneden, C., et al. 2008, ApJ, 675, 723
- Rosswog, S., Korobkin, O., Arcones, A., Thielemann, F.-K., & Piran, T. 2014, MNRAS, 439, 744
- Ryabchikova, T. A., Piskunov, N. E., Kupka, F., & Weiss, W. W. 1997, Baltic Astronomy, 6, 244
- Sackmann, I.-J., Boothroyd, A. I., & Kraemer, K. E. 1993, ApJ, 418, 457
- Simmerer, J., Sneden, C., Cowan, J. J., et al. 2004, ApJ, 617, 1091
- Sneden, C., Cowan, J. J., & Gallino, R. 2008, ARA&A, 46, 241
- Surman, R., McLaughlin, G. C., Ruffert, M., Janka, H.-T., & Hix, W. R. 2008, ApJ, 679, L117
- Travaglio, C., Galli, D., Gallino, R., et al. 1999, ApJ, 521, 691
- Travaglio, C., Gallino, R., Arnone, E., et al. 2004, ApJ, 601, 864
- Valenti, J. A. & Fischer, D. A. 2005, ApJS, 159, 141
- Valenti, J. A. & Piskunov, N. 1996, A&AS, 118, 595
- Winckler, N., Dababneh, S., Heil, M., et al. 2006, ApJ, 647, 685
- Woosley, S. E., Wilson, J. R., Mathews, G. J., Hoffman, R. D., & Meyer, B. S. 1994, ApJ, 433, 229

Appendix A: Complete linelists

In this section we listed the hfs components for the lines that suffer from hyperfine splitting.

Appendix B: Solar abundance plots

In Figs. B.1–B.5 the synthesis for all the lines analyzed in this work for the solar spectrum from Vesta observed at Magellan in January 2006 is shown. Each plot shows (in the bigger panel) the line fitting with the best fit to the observed one and the different abundances in steps of 0.04 dex. In the lower panel the differences between the observed spectrum and the synthetic one are shown, with the difference with the best fit highlighted. In the small square panel the χ^2 values for the different abundances are represented, with the red dot representing the minimum and therefore the best fit value for the elemental abundance.

Table A.1: Linelists for the synthesis of Sr. The lists include atomic data for Sr from [Bautista et al. \(2002\)](#) as well as additional lines nearby. Columns represent element line, wavelength and log(gf) values, respectively.

Sr II 4607		
Element	λ (Å)	log(gf)
Fe I	4607.0856	-3.530
Ni I	4607.1378	-2.759
Sr I	4607.3310	0.283
Nd II	4607.3800	-1.100
Mn I	4607.5880	-1.900

Table A.2: Linelists for the synthesis of Zr. The lists include atomic data for Zr from [Ljung et al. \(2006\)](#) as well as additional lines nearby. Columns represent element line, wavelength and log(gf) values, respectively.

Zr II 4208			Zr I 4687			Zr I 4739			Zr II 5112		
Element	λ (Å)	log(gf)	Element	λ (Å)	log(gf)	Element	λ (Å)	log(gf)	Element	λ (Å)	log(gf)
Th II	4208.8910	-0.738	Si I	4687.6210	-2.944	Mn I	4739.0870	-0.490	Fe I	5111.8550	-1.993
Cr I	4208.9529	-0.528	Fe I	4687.6700	-3.780	Ce II	4739.1470	-0.810	K I	5112.2460	-2.080
Zr II	4208.9800	-0.510	Zr I	4687.8090	0.550	Zr I	4739.4800	0.230	Zr II	5112.2700	-0.850
Cr II	4209.0941	-2.379	Ti I	4687.8090	-2.399	Ce II	4739.5190	-1.020	Sm II	5112.2930	-1.550
Cr I	4209.1730	-1.388	Fe I	4688.1770	-1.538	V I	4739.5750	-0.849	Cr I	5112.4850	-3.700

Table A.3: Linelists for the synthesis of La. The lists include the hfs (when available) of the La in question taken from [Ivans et al. \(2006\)](#) as well as additional lines nearby. Columns represent element line, wavelength and log(gf) values, respectively.

La II 4662			La II 4748			La II 5122			La II 6390		
Element	λ (Å)	log(gf)	Element	λ (Å)	log(gf)	Element	λ (Å)	log(gf)	Element	λ (Å)	log(gf)
Fe I	4662.0970	-4.751	Fe I	4748.0123	-2.544	C2 I	5122.8253	0.183	Fe I	6388.4047	-4.476
Cr I	4662.4020	-2.735	V I	4748.5030	-0.620	C2 I	5122.8948	0.175	Nd II	6389.9800	-0.770
La II	4662.4773	-2.951	La II	4748.7300	-0.540	La II	5122.9798	-1.476	La II	6390.4551	-2.012
La II	4662.4814	-2.511	Fe I	4749.0097	-3.058	La II	5122.9799	-2.046	La II	6390.4683	-2.752
La II	4662.4852	-2.240	Cr I	4749.2091	-1.643	La II	5122.9859	-2.046	La II	6390.4685	-2.183
La II	4662.4901	-2.252				La II	5122.9864	-1.888	La II	6390.4794	-3.752
La II	4662.4914	-2.136				La II	5122.9865	-1.874	La II	6390.4796	-2.570
La II	4662.4924	-2.256				La II	5122.9911	-1.888	La II	6390.4802	-2.390
La II	4662.5024	-2.511				La II	5122.9915	-2.556	La II	6390.4887	-3.330
La II	4662.5044	-2.056				La II	5122.9919	-1.899	La II	6390.4887	-2.536
Ce II	4662.6950	-0.850				La II	5122.9954	-1.899	La II	6390.4900	-2.661
Ti II	4662.7410	-3.429				La II	5122.9958	-3.999	La II	6390.4964	-3.100
						La II	5122.9962	-2.072	La II	6390.4971	-2.595
						La II	5122.9986	-2.072	La II	6390.4977	-3.079
						La II	5122.9990	-2.248	La II	6390.5021	-2.954
						C2 I	5123.1242	-0.410	La II	6390.5021	-2.857
						C2 I	5123.1796	-0.426	La II	6390.5058	-2.778
									Si I	6391.0205	-2.065
									Mn I	6391.2109	-1.491

Table A.4: Linelists for the synthesis of Ce. The lists include atomic data for Ce from [Lawler et al. \(2009\)](#) as well as additional lines nearby. Columns represent element line, wavelength and log(gf) values, respectively.

Ce II 4523			Ce II 4572			Ce II 4628			Ce II 5187		
Element	λ (Å)	log(gf)	Element	λ (Å)	log(gf)	Element	λ (Å)	log(gf)	Element	λ (Å)	log(gf)
Gd II	4522.8360	-0.310	Ti I	4572.0658	-1.361	Co I	4627.4250	-1.420	Ni I	5186.5527	-1.124
Sm II	4523.0300	-0.990	Cr II	4572.1870	-1.247	Fe I	4627.5471	-3.057	Fe I	5186.7543	-2.867
Ce II	4523.0750	-0.080	Ce II	4572.2780	0.220	Ce II	4628.1609	0.140	Ce II	5187.4578	0.170
Ti I	4523.2453	-1.848	Co II	4572.4616	-3.078	Ti I	4628.1842	-1.287	Ni I	5187.8199	-1.910
Mn I	4523.3952	-1.360	Ti I	4572.7676	-1.560	Ce II	4628.2391	-0.430	Fe I	5187.9142	-1.371

Table A.5: Linelists for the synthesis of Nd. The lists include the hfs (when available) of the Nd in question taken from [Roederer et al. \(2008\)](#) as well as additional lines nearby. Columns represent element line, wavelength and log(gf) values, respectively.

Nd II 4177			Nd II 4358			Nd II 4446			Nd II 5130			Nd II 5319		
Element	λ (Å)	log(gf)	Element	λ (Å)	log(gf)	Element	λ (Å)	log(gf)	Element	λ (Å)	log(gf)	Element	λ (Å)	log(gf)
Fe I	4177.0789	-3.369	CH I	4358.0000	-1.517	Fe II	4446.2433	-2.776	Cr I	5130.4239	-1.051	Fe I	5319.6228	-0.140
Fe II	4177.2014	-8.294	Fe I	4358.0763	-2.960	Fe I	4446.2747	-2.116	C2 I	5130.5777	-0.262	Fe I	5319.7629	-2.594
Nd II	4177.2885	-4.315	Nd II	4358.1255	-3.132	Nd II	4446.3635	-4.140	Nd II	5130.5900	0.450	Nd II	5319.8100	-0.140
Nd II	4177.2948	-2.865	Nd II	4358.1346	-1.821	Nd II	4446.3647	-3.935	Fe I	5130.9095	-2.818	Fe I	5320.0356	-2.540
Nd II	4177.2984	-3.927	Nd II	4358.1351	-2.908	Nd II	4446.3648	-3.141	Ce II	5131.1908	-2.470	Cr I	5320.4280	-1.527
Nd II	4177.3021	-1.717	Nd II	4358.1433	-1.909	Nd II	4446.3657	-2.690						
Nd II	4177.3025	-4.487	Nd II	4358.1438	-2.820	Nd II	4446.3664	-2.930						
Nd II	4177.3039	-2.647	Nd II	4358.1455	-3.299	Nd II	4446.3665	-3.908						
Nd II	4177.3064	-3.032	Nd II	4358.1501	-0.725	Nd II	4446.3677	-2.571						
Nd II	4177.3074	-2.736	Nd II	4358.1511	-1.989	Nd II	4446.3686	-2.835						
Nd II	4177.3087	-4.096	Nd II	4358.1512	-1.977	Nd II	4446.3690	-3.986						
Nd II	4177.3102	-1.802	Nd II	4358.1514	-3.075	Nd II	4446.3703	-2.453						
Nd II	4177.3109	-1.884	Nd II	4358.1517	-2.799	Nd II	4446.3714	-2.799						
Nd II	4177.3120	-2.564	Nd II	4358.1524	-3.132	Nd II	4446.3722	-4.177						
Nd II	4177.3121	-2.814	Nd II	4358.1566	-2.076	Nd II	4446.3735	-2.342						
Nd II	4177.3143	-3.904	Nd II	4358.1569	-2.987	Nd II	4446.3749	-2.814						
Nd II	4177.3154	-3.658	Nd II	4358.1581	-2.086	Nd II	4446.3750	-4.289						
Nd II	4177.3160	-1.969	Nd II	4358.1586	-2.830	Nd II	4446.3758	-4.289						
Nd II	4177.3161	-0.665	Nd II	4358.1594	-2.908	Nd II	4446.3762	-5.565						
Nd II	4177.3172	-2.732	Nd II	4358.1597	-0.783	Nd II	4446.3763	-2.857						
Nd II	4177.3175	-1.892	Nd II	4358.1614	-2.165	Nd II	4446.3768	-4.098						
Nd II	4177.3192	-0.723	Nd II	4358.1617	-2.966	Nd II	4446.3769	-4.054						
Nd II	4177.3193	-2.549	Nd II	4358.1622	-3.299	Nd II	4446.3773	-2.238						
Nd II	4177.3194	-3.824	Nd II	4358.1642	-2.172	Nd II	4446.3774	-0.915						
Nd II	4177.3196	-0.864	Nd II	4358.1647	-2.925	Nd II	4446.3777	-2.739						
Nd II	4177.3206	-2.059	Nd II	4358.1655	-2.820	Nd II	4446.3782	-3.002						
Nd II	4177.3216	-2.716	Nd II	4358.1658	-2.254	Nd II	4446.3785	-4.154						
CN I	4177.3222	-1.091	Nd II	4358.1661	-2.997	Nd II	4446.3791	-2.897						
Nd II	4177.3223	-3.685	Nd II	4358.1666	-3.075	Nd II	4446.3793	-2.621						
Nd II	4177.3235	-3.852	Nd II	4358.1686	-0.924	Nd II	4446.3800	-2.966						
Nd II	4177.3251	-1.344	Nd II	4358.1693	-2.250	Nd II	4446.3805	-4.346						
Nd II	4177.3238	-1.988	Nd II	4358.1695	-2.370	Nd II	4446.3813	-2.509						
Nd II	4177.3245	-2.155	Nd II	4358.1699	-3.093	Nd II	4446.3817	-2.142						
Nd II	4177.3253	-2.585	Nd II	4358.1700	-3.149	Nd II	4446.3821	-2.982						
Nd II	4177.3254	-2.572	Nd II	4358.1703	-2.987	Nd II	4446.3829	-0.973						
Nd II	4177.3271	-4.059	Nd II	4358.1706	-2.799	Nd II	4446.3829	-4.737						
Nd II	4177.3278	-2.259	Nd II	4358.1727	-2.417	Nd II	4446.3836	-2.405						
Nd II	4177.3281	-3.890	Nd II	4358.1731	-3.316	Nd II	4446.3837	-2.051						
Nd II	4177.3283	-1.352	Nd II	4358.1735	-2.966	Nd II	4446.3840	-3.115						
Nd II	4177.3285	-2.848	Nd II	4358.1736	-2.311	Nd II	4446.3847	-3.064						
Nd II	4177.3291	-2.092	Nd II	4358.1749	-2.830	Nd II	4446.3864	-2.309						
Nd II	4177.3303	-2.680	Nd II	4358.1754	-2.478	Nd II	4446.3878	-3.282						
Nd II	4177.3304	-2.371	Nd II	4358.1762	-2.997	Nd II	4446.3882	-1.114						
Nd II	4177.3308	-3.059	Nd II	4358.1771	-2.341	Nd II	4446.3896	-2.219						
Nd II	4177.3322	-2.489	Nd II	4358.1775	-2.508	Nd II	4446.3928	-1.967						
Nd II	4177.3333	-2.607	Nd II	4358.1783	-2.925	Nd II	4446.3932	-2.134						
Nd II	4177.3334	-2.203	Nd II	4358.1783	-3.093	Nd II	4446.3937	-1.594						
Nd II	4177.3341	-2.891	Nd II	4358.1784	-1.404	Nd II	4446.4000	-1.602						
Nd II	4177.3363	-2.321	Nd II	4358.1799	-3.316	Fe I	4446.4786	-3.963						
Nd II	4177.3382	-2.440	Nd II	4358.1808	-3.149	Gd II	4446.4786	-1.280						
CN I	4177.3480	-1.123	Nd II	4358.1912	-1.412									
Ti I	4177.3790	-1.900	CH I	4358.2170	-1.412									
			Fe II	4358.3674	-7.807									

Table A.6: Linelists for the synthesis of Sm. The lists include the hfs (when available) of the Sm in question taken from [Lawler et al. \(2006\)](#) and [Roederer et al. \(2008\)](#) as well as additional lines nearby. Columns represent element line, wavelength and log(gf) values, respectively.

Sm II 4467			Sm II 4523			Sm II 4577			Sm II 4669		
Element	λ (Å)	log(gf)	Element	λ (Å)	log(gf)	Element	λ (Å)	log(gf)	Element	λ (Å)	log(gf)
Gd II	4467.2260	-0.848	Nd II	4522.8220	-1.080	V I	4577.1741	-1.048	Sm II	4669.3900	-0.600
Cr I	4467.3154	-2.193	Gd II	4522.8360	-0.310	Fe I	4577.6736	-3.465	Ce II	4669.4997	-0.410
Sm II	4467.3135	-1.957	Sm II	4523.0300	-0.990	Sm II	4577.6900	-0.650	Sm II	4669.6400	-0.530
Sm II	4467.3146	-2.682	Ce II	4523.0750	-0.080	Fe II	4577.7803	-5.237	Cr I	4669.6642	-2.268
Sm II	4467.3160	-3.896	Ti I	4523.2453	-1.848	Mn I	4578.0555	-1.185	Fe I	4669.9606	-2.108
Sm II	4467.3173	-1.874									
Sm II	4467.3188	-2.464									
Sm II	4467.3189	-1.993									
Sm II	4467.3200	-2.717									
Sm II	4467.3207	-3.662									
Sm II	4467.3215	-3.931									
Sm II	4467.3222	-1.788									
Sm II	4467.3223	-1.909									
Sm II	4467.3236	-2.499									
Sm II	4467.3241	-2.370									
Sm II	4467.3255	-3.698									
Sm II	4467.3263	-1.823									
Sm II	4467.3265	-3.614									
Sm II	4467.3281	-1.704									
Sm II	4467.3282	-2.405									
Sm II	4467.3303	-3.651									
Sm II	4467.3305	-2.338									
Sm II	4467.3314	-1.739									
Sm II	4467.3335	-3.683									
Sm II	4467.3336	-2.373									
Sm II	4467.3352	-1.623									
Sm II	4467.3360	-3.716									
Sm II	4467.3373	-1.658									
Sm II	4467.3382	-2.348									
Sm II	4467.3382	-1.363									
Sm II	4467.3398	-2.394									
Sm II	4467.3406	-0.799									
Sm II	4467.3408	-0.982									
Sm II	4467.3410	-0.423									
Sm II	4467.3418	-3.863									
Sm II	4467.3420	-0.493									
Sm II	4467.3426	-3.901									
Sm II	4467.3434	-1.545									
Sm II	4467.3441	-1.581									
Sm II	4467.3469	-2.480									
Sm II	4467.3471	-2.445									
Sm II	4467.3500	-4.282									
Sm II	4467.3514	-4.248									
Sm II	4467.3518	-1.507									
Sm II	4467.3529	-1.471									
Sm II	4467.3549	-2.703									
Sm II	4467.3572	-2.668									
Sm II	4467.3603	-1.437									
Sm II	4467.3636	-1.401									
Fe I	4467.4254	-2.655									
Co I	4467.4773	-1.412									

Table A.7: Linelists for the synthesis of Eu II. The lists include the hfs of the Eu II in question taken from [Lawler et al. \(2001\)](#) as well as additional lines nearby. Columns represent element line, wavelength and log(gf) values, respectively.

Eu II 4129		
Element	λ (Å)	log(gf)
CN I	4129.6006	-0.585
Eu II	4129.5966	-1.833
Eu II	4129.6001	-1.356
Eu II	4129.6137	-1.637
Eu II	4129.6185	-1.298
Eu II	4129.6220	-1.833
Eu II	4129.6387	-1.578
Ti I	4129.6429	-1.424
Eu II	4129.6444	-1.167
Eu II	4129.6492	-1.637
Eu II	4129.6716	-1.614
Eu II	4129.6774	-1.795
Eu II	4129.6781	-1.017
Eu II	4129.6801	-1.318
Eu II	4129.6838	-1.598
Eu II	4129.6839	-1.578
Eu II	4129.6871	-1.260
Eu II	4129.6898	-1.795
Eu II	4129.6941	-1.539
Eu II	4129.6977	-1.129
Eu II	4129.7007	-1.598
Eu II	4129.7117	-0.979
Eu II	4129.7130	-1.801
Eu II	4129.7150	-1.539
Eu II	4129.7198	-0.866
Eu II	4129.7240	-1.576
Eu II	4129.7263	-1.614
Eu II	4129.7295	-1.763
Eu II	4129.7305	-0.828
Eu II	4129.7331	-1.576
Eu II	4129.7548	-0.683
Eu II	4129.7558	-1.763
Eu II	4129.7769	-1.801
Eu II	4129.7700	-0.721
Nd II	4129.8370	0.180
Co I	4129.8421	-1.587

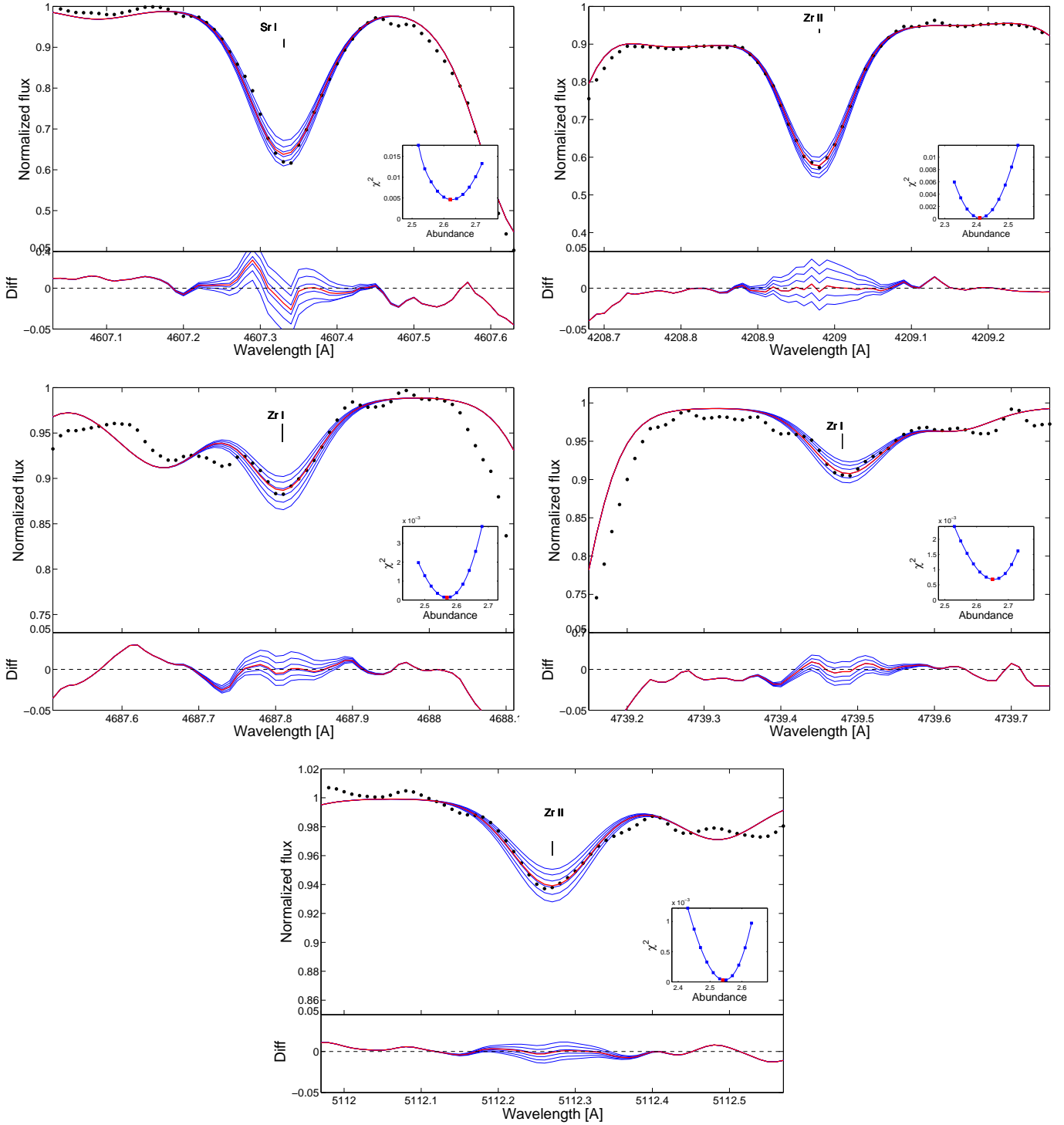


Fig. B.1: Solar spectrum taken using asteroid Vesta during run at Magellan in January 2006. Spectral lines are listed in order of element and wavelength. Chemical elements with all the hfs lines are indicated inside the lines. The different colored lines are the different synthetic spectra with different abundances in steps of 0.04 dex, while the dots are the observed spectra. In the lower panels are the values of differences between the real and synthetic spectra for the synthetic spectra plotted above. The red lines represent the best fit derived from unnormalized χ^2 , visible in the small plot as a red dot. Here the fits for the Sr line and the five Zr lines are shown.

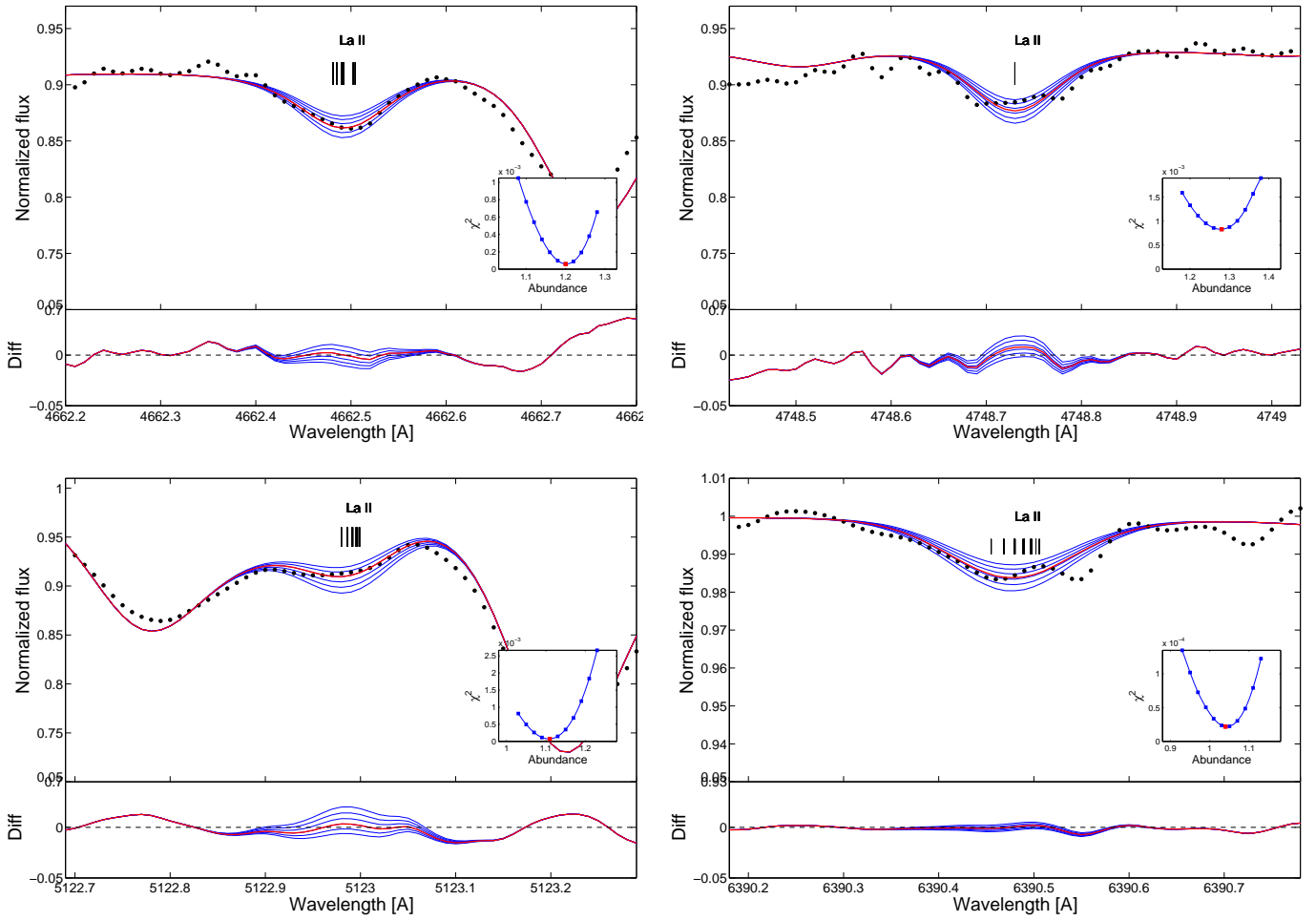


Fig. B.2: As in Fig. B.1 but for the four La lines.

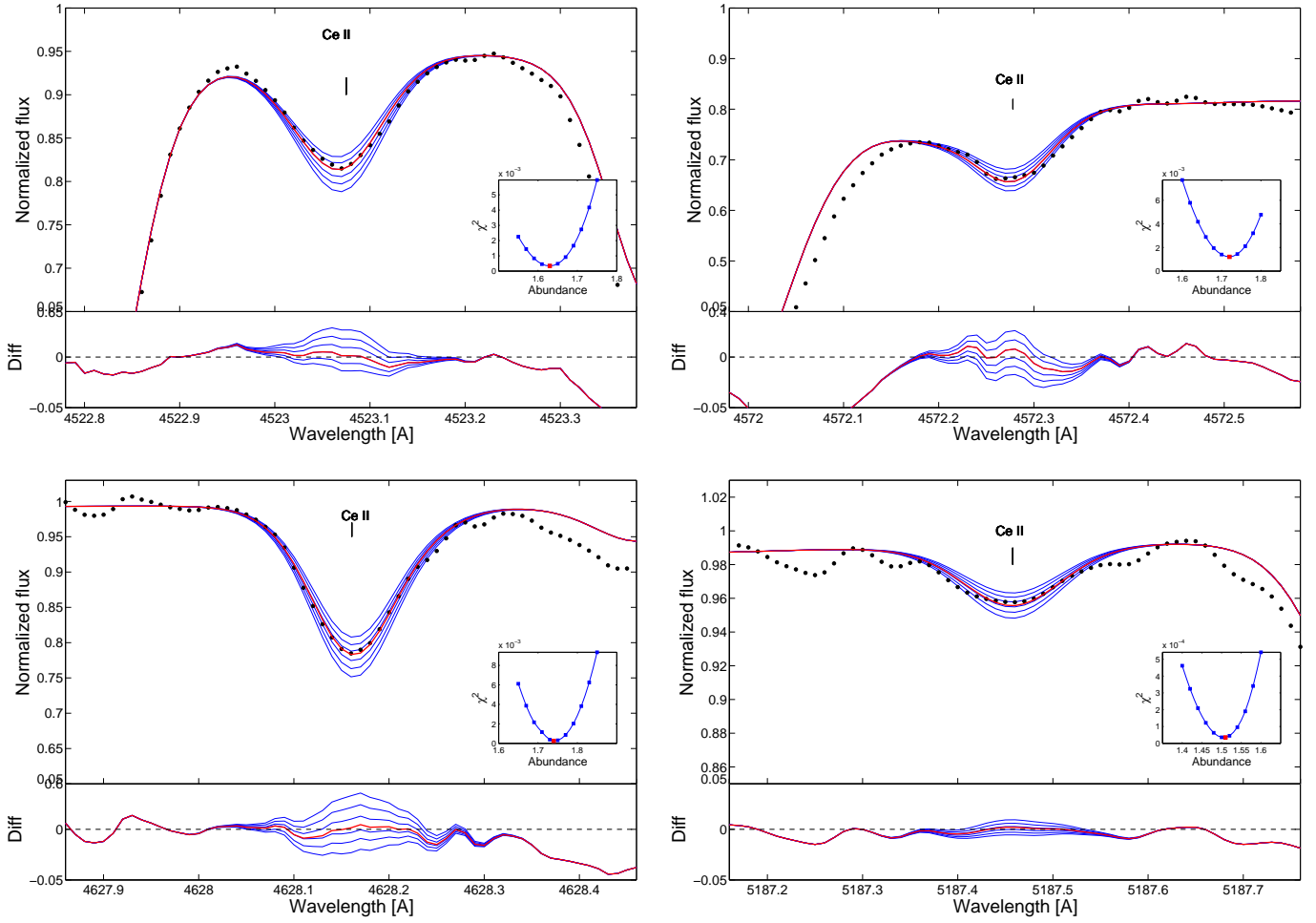


Fig. B.3: As in Fig. B.1 but for the four Ce lines.

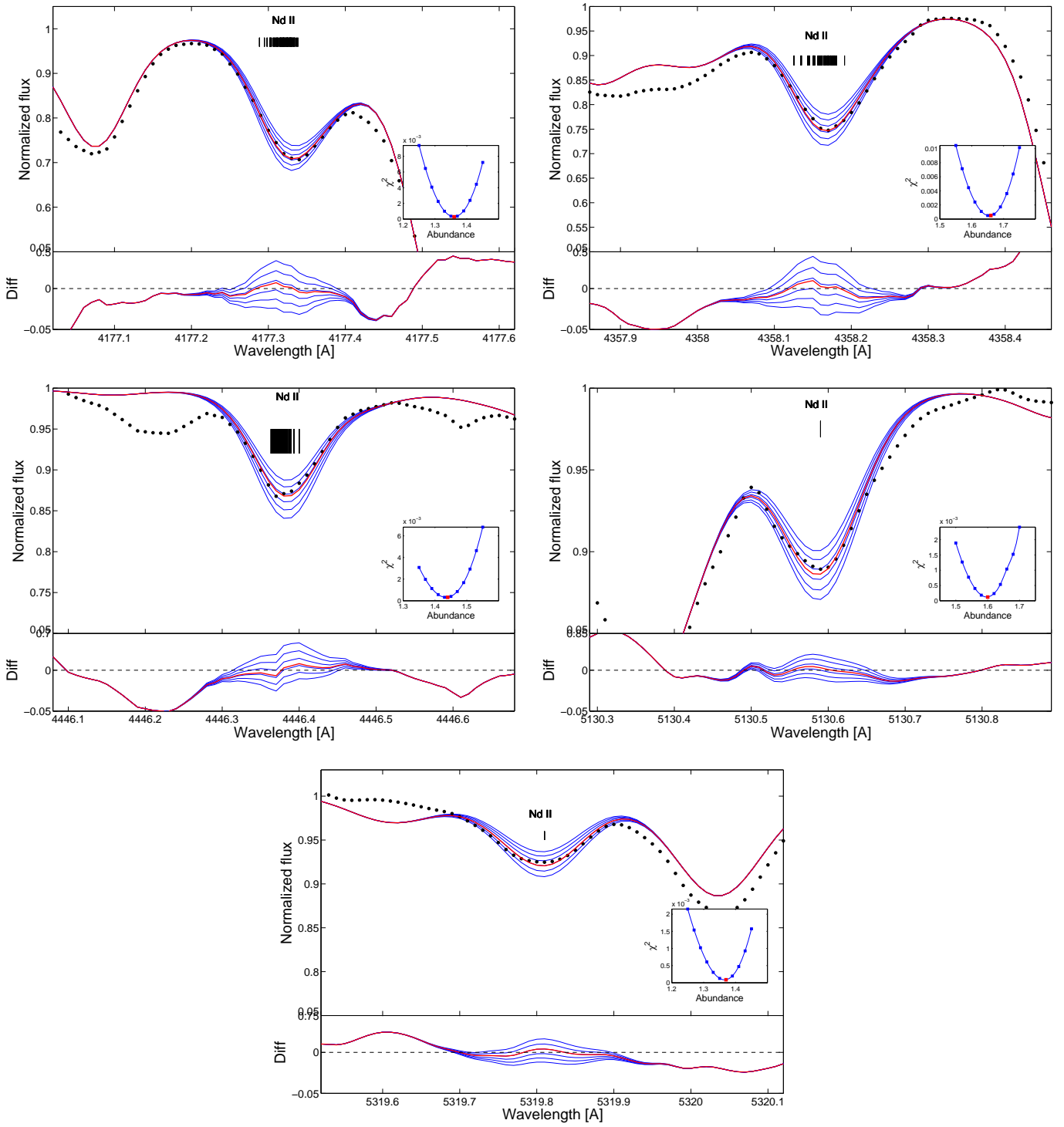


Fig. B.4: As in Fig. B.1 but for the five Nd lines.

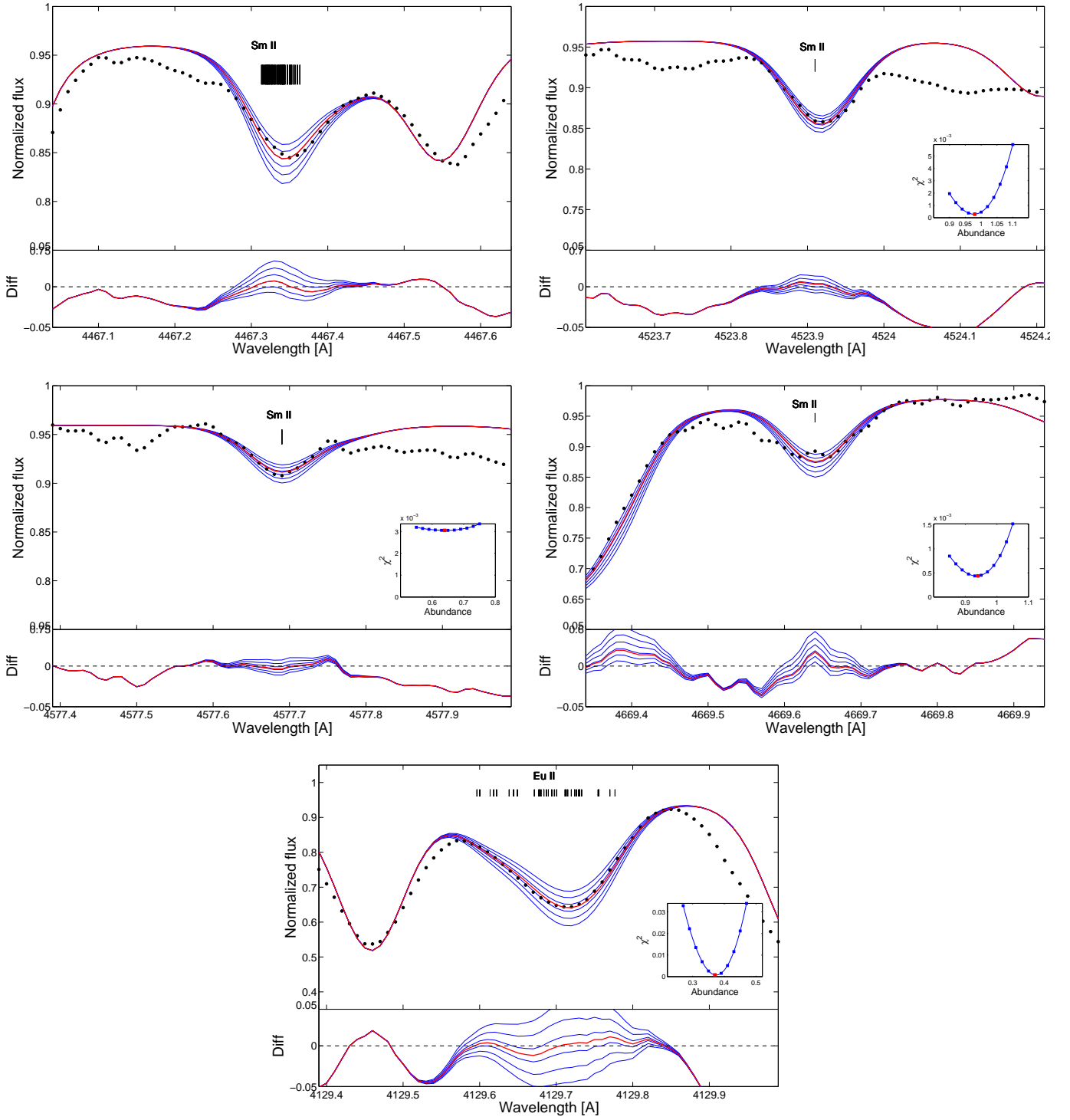


Fig. B.5: As in Fig. B.1 but for the four Sm lines and the two Eu lines.